Qinglong Zhao

The influence of Mn, Fe and Si on the work hardening of aluminum alloys

Thesis for the degree of Philosophiae Doctor

Trondheim, February 2013

Norwegian University of Science and Technology
Faculty of Natural Sciences and Technology
Department of Materials Science and Engineering

NTNU – Trondheim
Norwegian University of
Science and Technology

NTNU
Norwegian University of Science and Technology

Thesis for the degree of Philosophiae Doctor

Faculty of Natural Sciences and Technology
Department of Materials Science and Engineering

ISBN 978-82-471-4121-2 (printed ver.)
ISBN 978-82-471-4122-9 (electronic ver.)
ISSN 1503-8181

Doctoral theses at NTNU, 2013:16

IMT-Report 2013:172

Printed by NTNU-trykk

Preface

This thesis is submitted in fulfillment of the requirements for the doctor of philosophy at Norwegian University of Science and Technology (NTNU). The work has been carried out at the Department of Materials Science and Engineering (DMSE), NTNU from March 2010 to November 2012. Professor Bjørn Holmedal at DMSE, NTNU was the main supervisor. Yanjun Li at SINTEF Materials and Chemistry and Professor Knut Marthinsen at DMSE, NTNU were co-supervisors. The thesis consists of two parts. The first part includes the introduction, literature review and summary of the work. The second part contains five articles which present the main work of the PhD thesis.

Publications contained in this thesis:

1. "Influence of dispersoids on microstructure evolution and work hardening of aluminum alloys", submitted to *Philosophical Magazine*;

2. "Modeling work hardening of aluminum alloys containing dispersoids", submitted to *Philosophical Magazine*;

3. "Comparison of the influence of Si and Fe in 99.999% purity aluminum and in commercial-purity aluminum", *Scripta Materialia* 67 (2012) 217-220;

4. "The effect of silicon on the strengthening and work hardening of aluminum at room temperature", *Materials Science & Engineering A* 563 (2013) 147-151;

5. "Effect of Si additions on solid solution hardening of Al-Mn alloys", 13th International Conference on Aluminum Alloys (ICAA13), Pittsburgh, USA, 3-7 June, 2012, doi: 10.1002/9781118495292.ch273.

A full list of publications will be found on the website:
http://www.researcherid.com/rid/B-3724-2008.

Abstract

The relationship between the processing, the structure and the properties is a key issue in materials science research. The improvement of the properties and optimization of the process always requires a better understanding of their relationship. For instance, the mechanical properties are essential for structural materials. The objective of this thesis is to investigate the influence of structural variables, i.e. dispersoids and solutes, on the strengthening and work hardening behavior of aluminum alloys.

An Al-Mn-Fe-Si model alloy was used to investigate the influence of dispersoids on work hardening. This model alloy had similar composition as the commercial AA3103 alloy. After homogenization, the alloy contains fine dispersoids, coarse constituent particles and solutes in solid solution. Therefore, this alloy provides a complex system to study, which is of academic and industrial interest. The work hardening behavior of as-homogenized and cold-rolled alloys was tested by tension at room temperature. The corresponding microstructure was characterized by transmission and scanning electron microscopes. The strengthening mechanisms during deformation were discussed, including Orowan stress and internal stress. It is found that a high density of fine dispersoids strengthens the alloy significantly, but their effect diminishes as strain increases. The work hardening rate is increased due to extra dislocations induced by dispersoids during the initial deformation, but it is reduced at larger strains. After experimental investigation of the effect of dispersoids on work hardening, it was attempted to model their effect. A simplified model of dislocation evolution influenced by dispersoids was proposed.

Solid solution hardening has been investigated for decades, but the mechanisms in a multi-component solid solution have not yet been fully clarified. Commercial aluminum alloys usually contain several alloying elements besides trace elements. The effect of each element and the interaction between these elements are however not well understood. The effect of trace elements on the strengthening of commercially pure aluminum was investigated in this work. A high-purity base aluminum with addition of Si and Fe was compared to a commercial-purity aluminum containing similar content of

Si and Fe. Their mechanical properties are found to be similar, suggesting that trace elements play a minor role in strengthening.

Solute strengthening in Al-Si alloys of commercial purity was also investigated by tensile testing of several Al-Si alloys with various compositions at room temperature. The effect of Si on strengthening and work hardening was quantitatively characterized. Quenching is found to affect the solution hardening at small strains. After a study on solute strengthening in binary alloys, solute strengthening in alloys containing several elements can be studied. The multi-component hardening was investigated by comparison of an Al-Mn-Si ternary alloy and Al-Mn binary alloys. The multi-component superposition is usually applied under the assumption of no interaction between each element. However, the present experimental results suggest that this simple superposition can not explain the hardening in the ternary alloy. Clustering is assumed to cause the hardening in the case of the ternary alloy.

Acknowledgements

I am grateful to my principal supervisor Bjørn Holmedal for his professional guidance, and also to my co-supervisors Yanjun Li and Knut Marthinsen for their helpful discussions and suggestions. The financial support from the Research Council of Norway, Hydro and Sapa is acknowledged.

The co-author of the third article, Marius Slagsvold was a Master student at DMSE, NTNU, who graduated in June 2011. He worked on the recrystallization and tension tests of high-purity aluminum. The tensile test results from his Master thesis were incorporated in the third article. His contribution is acknowledged.

I would like to thank the staff for their technical assistance: Yingda Yu, Torild Krogstad, Morten Raanes, and especially Pål Christian Skaret, with whom I did plenty of mechanical tests.

I want to thank my colleagues sharing my office: Ning Wang, Sindre Bunkholt and Nagaraj Vinayagam Govindaraj. We had three years together of hope and disappointment, joy and distress. We helped each other with the PhD life. There are also many other colleagues to be acknowledged: Kai Zhang, Tomas Manik, Emmanuel Hersent, Sapthagireesh Subbarayan et al., who brought fun to life. Many Chinese friends of mine also deserve my appreciation, who help with my daily life in Trondheim.

Finally I wish to dedicate the thesis to my parents for their approval of my study abroad, even though they are not interested in nor understand my work.

Contents

Chapter 1 Introduction

1.1 Background

One of many global challenges facing humanity is sustainable development and climate change (according to Millennium Project). Sustainable development demands sustainable use of materials, i.e. recycling of materials is necessary for both sustainable development and environmental protection. Aluminum and its alloys are one of the main structural materials. They are widely used, especially in transportation, containers and packaging, which consumed ~50% of aluminum in North America in 2010 and 2011. Moreover, the demand of aluminum is increasing, especially for the applications in vehicles. The transport sector is responsible for a large share of global greenhouse gas emissions. For example, the transport sector was the second largest source of emissions in USA in 2010 (from EPA). Road transport is the largest contributor in transportation [1]. One way to reduce emissions in transportation is the application of lightweight materials to build vehicles, such as aluminum. To meet both the sustainable use and increasing demands, recycled aluminum has become an important source of aluminum production. For example, about 40% of the production in USA in 2011 is recycled aluminum (from USGS: Aluminum - Mineral Commodity Summary 2012). However, the worldwide production of recycled aluminum in 2010 is 8.4 million tons, only 16% of the total production (from GDA).

An increased use of recycled aluminum requires the development of new tailor made alloys and an optimization of the thermo-mechanical processing routes so that to handle the corresponding changes and variations of chemical compositions (alloying elements and impurities). However, the traditional plant trials to meet this challenge are both costly and time-consuming. Advanced mathematical modeling tools are believed to be a powerful tool to predict the microstructure evolution during thermo-mechanical processing. To meet the aluminum industry's need for accurate and efficient tools for analysis, design and optimization of alloys, processes and products based on recycled aluminum, an in-depth scientific understanding and quantitative relationship of

processing–structure–property are needed. Aluminum is usually used as a structural material, so its mechanical properties are essential. Present work focuses on the relationship between microstructure and strength.

1.2 Objectives

The strengthening mechanisms in aluminum alloys include work hardening, solid solution hardening, dispersion/precipitation hardening and grain boundary hardening. These strengthening mechanisms may interact with each other during deformation. In commercial alloys, alloying elements may form dispersoids or precipitates during heat treatments, while the remaining elements are in solid solution. Both dispersoids /precipitates and solutes can strengthen the alloys and affect the work hardening behavior during deformation. The commercial alloy contains several alloying elements, and the quantitative prediction needs to characterize the strengthening contribution of each element. The complicated system of reality requires the understanding not only of each strengthening component, but also of the interactions between strengthening components. Thus, the objectives of the present work are:

1) Investigation of the influence of dispersoids on work hardening behavior;
2) A quantitative characterization of solid solution hardening;
3) Investigation of solid solution hardening of multi-component aluminum alloys.

The experimental work involves the characterization of microstructure and testing of mechanical properties. The classical theories are reconsidered and simplified models are developed for the model alloys.

Chapter 2 Literature review

Work hardening, also known as strain hardening, is the strengthening of a metal by plastic deformation. Work hardening manifests itself macroscopically as an increase in the flow stress with increasing plastic strain in a stress-strain test, or as an increase in the hardness in an indentation test. This strengthening occurs because of dislocation movement, interaction and accumulation within the crystal structure of the material.

2.1 The theories of strengthening and work hardening

2.1.1 Work hardening

The plasticity of crystalline materials at room temperature is usually based on dislocation glide. Stress-strain curves tend to exhibit four recognizable "stages", as indicated in Fig. 2.1.1, each associated with its own characteristic type of dislocation structure. Stage I is referred to as easy glide, which is often observed in single-crystals and HCP crystals. Stage II is related to the storage of dislocations, which is independent of temperature. Dynamic recovery starts at the beginning of stage III, which reduces the storage of dislocations. A cell structure forms in stage III, and continues to refine in stage IV. At very large strains, stage IV is terminated by a saturation of hardening at stage V. Polycrystalline fcc metals usually exhibit only stage II and III in tensile tests. Readers can find more details in some reviews [2-4].

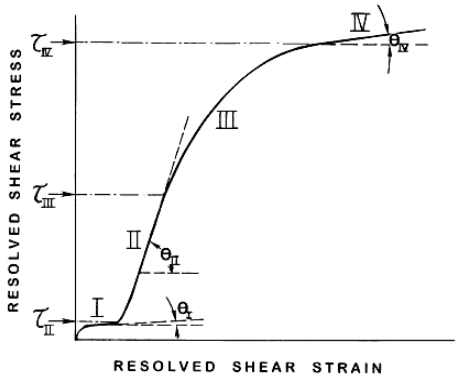

Figure 2.1.1 Idealized four-stage work hardening curve.

A basic agreement in models is that flow stress is proportional to the square root of dislocation density, which is confirmed by experiments. Kocks, Mecking and Estrin developed a one-parameter approach of work hardening, where the only structure parameter is dislocation density [5-6]. This model produces the same stress-strain curves as the Voce equation. Kocks and Mecking [4] refined their model of dynamic recovery, giving a better physical interpretation. Kuhlmann-Wilsdorf [7-8] proposed a mesh-length theory originally from Taylor theory. The model features a low energy dislocation structure formed during deformation. The dislocation density is scaled with cell size by a similitude law.

The NTNU group [9-10] has developed a unified microstructural metal plasticity (MMP) model applicable in testing and processing of aluminum alloys. This model relies on a multi-parameter description for the microstructure evolution. At small strains the stored dislocations are arranged in a cell structure characterized by cell size, cell-wall thickness, and dislocation densities within walls and within cells. At large strains cell walls collapse into sub-boundaries of a well defined misorientation. Dynamic recovery is treated similar to static recovery, following the Bailey-Orowan approach. The annihilation mechanism involves collapse of edge dipoles [10]. It should be noted that Kocks and Mecking [4] disapprove this treatment of dynamic recovery.

2.1.2 Solid solution hardening

The work hardening mechanisms are based on dislocations, i.e. dislocation interaction, arrangement and density. Therefore, the solid solution strengthening is also explained based on the concept of dislocations. No great increase in grown-in dislocation density due to solute addition was observed [11]. High content of solute can decrease the stacking-fault energy, leading to more difficulty in cross slip. But this solute effect on stacking-fault energy can be neglected in dilute alloys. The dislocation-solute interactions play an important role in work hardening. And this mechanism will be discussed later. As the hardening mechanism might be different between different crystal structures and nature of solutes, the discussion of solute hardening in this review is confined to the substitutional alloys of face-centered cubic (FCC) structure.

The interaction of a dislocation with a solute atom

The cause of the dislocation-solute interactions is that solute atoms change the periodical matrix lattice locally, like defects. The dislocations do not move in the same relative perfect periodical lattice as they do in the pure materials. The interaction energy between a dislocation and a solute atom can be due to: 1) the strain fields (the size difference between solute and solvent, i.e. size misfit); 2) the different bonding around the solute (like elastic modulus misfit) [12]. The corresponding glide force on a dislocation can be calculated under the assumption of rigid and linear isotropic elasticity of dislocations. The maximum force on the edge dislocation is given by

$$f_m^s = \frac{81\mu\Omega}{16\pi ab\sqrt{3}}\frac{\mathrm{d}a}{\mathrm{d}c} \approx \mu b^2\delta, \qquad (1)$$

where Ω is the atomic volume, a is the lattice parameter, c is the concentration of solutes, and δ is the size misfit parameter, $\delta = \frac{\mathrm{d}a}{a\cdot\mathrm{d}c}$. In the same approximation, a screw dislocation has no interaction with a spherically symmetrical strain field because it has a pure shear strain field [12]. But a force due to elastic modulus misfit will act on a screw dislocation. The maximum force is given by

$$f_m^\mu = \frac{27\sqrt{2}\mu\Omega}{256\pi^2 b\mu}\frac{\mathrm{d}\mu}{\mathrm{d}c} \approx \frac{\mu b^2\eta}{60} \qquad (2)$$

where η is the modulus misfit parameter, $\eta = \frac{\mathrm{d}\mu}{\mu\mathrm{d}c}$ [12]. Although the force due to the size misfit in the equation appears much larger than that due to the modulus misfit, these two forces are often comparable because the modulus misfit is often much larger than the size misfit. For instance, the size misfit and modulus misfit of Cu-Al alloys are about 0.067 and 0.58 (polycrystal), respectively [13]. It should be noted that the maximum forces calculated here are in the conditions without any thermal assistance, so they are the forces at 0 K and will be reduced at elevated temperatures.

The different bonding around the solute does not include only elastic modulus misfit, but also the difference in electron density around the solute and segregation of solutes in the stacking faults of extended dislocations. Cottrell electrostatic locking and Suzuki

chemical locking explain these interactions (more details in [13-14]). They are relatively less important in dilute aluminum alloys, so they are not discussed here.

Dislocation-solute interaction mechanisms

The dislocation-solute interactions can be subdivided into two mechanism groups [14]:

i) Solute atoms, which collect on dislocations at rest, and drag/lock the dislocation.

ii) Stationary solute atoms act on moving dislocations like friction.

If the solutes can diffuse to the favorable positions around dislocations (at relatively high temperature), the locking mechanism is preferred, and a yield point should be observed, such as dynamic strain aging. In low temperature regions, solutes are more stationary and act like obstacles on moving dislocations. The distribution of solutes /obstacles and how obstacles interact with dislocations are important. It has been treated as two cases, defined by a dimensionless parameter, η_0 [14-15].

$$\eta_0 = \frac{w}{l_s}\left(\frac{2\Gamma}{f_m}\right)^{1/2} \tag{3}$$

w is the range of interactions, l_s is the average distance between obstacles in the plane or l_s^2 is average area of slip plane per obstacle, $l_s \approx \frac{b}{\sqrt{c}}$, Γ is dislocation line tension, and f_m is the maximum interaction force defined in the last section.

If $\eta_0 << 1$, the interaction is treated by Fleischer-Friedel statistics for dilute, strong point obstacles (Fig. 2.1.2-1a). If $\eta_0 > 1$, it is treated by Mott-Labusch statistics for concentrated, weak obstacles (Fig. 2.1.2-1b).

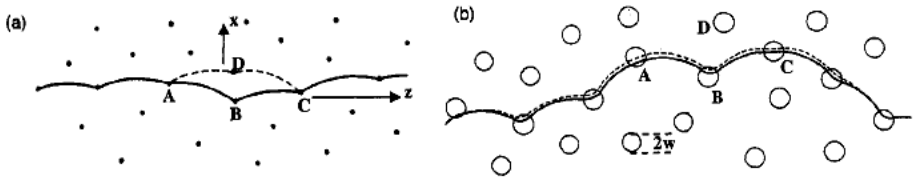

Fig. 2.1.2-1 (a) Fleischer-Friedel statistics. The unit step is the breakaway of the dislocation from the point obstacle B until the segment AC stops at the obstacle D. No motion outside AC occurs. (b) Mott-Labusch statistics. The dislocation is attracted to diffuse obstacles of width 2w. When the dislocation breaks away from obstacle B, it moves forward in other segments outside AC. [12]

Fleischer-Friedel statistics

The Fleischer-Friedel statistics is valid for small isolated obstacles of high strength. All obstacles oppose the dislocation motion and the dislocation bows out between them, as illustrated in Fig. 2.1.2-1a. The obstacles are touched by the dislocations at full interaction force or not at all. An experimental example is shown in Fig. 2.1.2-2.

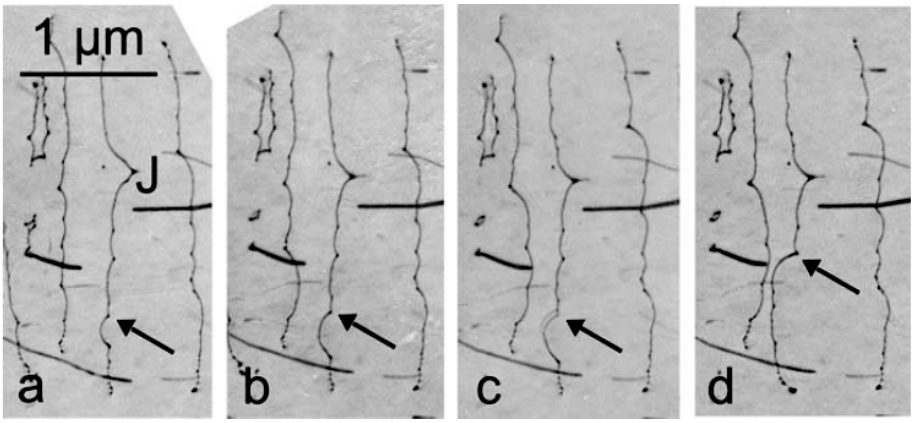

Fig. 2.1.2-2 Dislocations in a MgO single crystal overcoming localized obstacles during in situ deformation in an HVEM at room temperature (quoted by [16]).

The Fleischer-Friedel stress at 0 K is [17]

$$\hat{\tau} = \frac{f_m^{3/2}}{lb}\left(\frac{c}{2\Gamma}\right)^{1/2}. \qquad (4)$$

Γ is line tension of dislocations, l^2 is the area per atom on the slip plane, $l^2 = b^2\frac{\sqrt{3}}{4c}$ [18].

Mott-Labusch statistics

The dislocation is in touch with obstacles on both the entrance and the exit sides of their force–distance curves. Thus, the obstacles cause forces on the dislocation in the forward and backward directions. According to [18], the threshold shear resistance in this case is

$$\hat{\tau} = 1.26\mu\left(\frac{w}{b}\right)^{1/3} c^{2/3}\left(\frac{f_m}{2\Gamma}\right)^{4/3}. \qquad (5)$$

Temperature dependency

The temperature dependency of critical shear stress can be calculated by assuming the force—distance profile. Generally, [12, 14]

$$\left(\frac{\tau}{\hat{\tau}}\right)^{p} = 1-\left(\frac{T}{T_0}\right)^{q} \text{ with } kT_0 = f_m w / \ln\left(\dot{\varepsilon}_0 / \dot{\varepsilon}\right). \quad (6)$$

The values of p and q will vary according to different assumptions, such as p=q=2/3 for a parabolic force-distance curve, or p=1 and q=2/3 in Labusch theory. Leyson et al. [19] used a different equation, which is more consistent with the experiments at elevated temperatures.

2.1.3 Precipitation hardening

The strengthening mechanism is complicated because of the complicated nature of dispersed particles. The strengthening can be due to interface, stacking fault, modulus, or coherency [20-21]. The simplification can be achieved by treating particles as two types, i.e. shearable or non-shearable. The dislocation will bow out when it meets a point obstacle. The contact angle between two dislocation segments, φ, should be 0-π. The maximum force on an obstacle by a dislocation is 2Γ when the angle φ=0. If the obstacle is very strong, f_m> 2Γ, the dislocation will bypass it and leave a loop. Thus, the strong obstacles always affect work hardening by athermal storage of dislocations. The interaction of dislocations with the precipitates usually depends on the level of coherency between the precipitate and the matrix. If the precipitate is coherent with the matrix, the matrix dislocations will be able to shear the precipitate by planar slip. On the other hand, when the precipitates are incoherent with the matrix lattice planes, they are probably non-shearable to the dislocations. The dislocation will have to bypass the obstacle by bowing out between the precipitates, by cross slip or climb, to an alternate slip system. In this case, the presence of precipitates increases the dislocation density in comparison to an alloy without precipitates (at similar strains) due to the accumulation of geometrically necessary dislocations around these particles.

The particles which interact with dislocations can be treated as localized obstacles or extended obstacles, which are very similar to Friedel and Mott statistics in the solid

solution hardening part. Generally, the precipitate particles are strong but not numerous, so they can be treated as strong points, like Friedel statistics. When the particles are relatively weak, which is expected to be valid for underaged alloys, the critical shear stress is written as

$$\hat{\tau} = \frac{f_m^{2/3}}{bL_s\left(2\Gamma\right)^{1/2}}. \tag{7}$$

L_s is the average area occupied per obstacle on the glide plane, $L_s = \left(\frac{2\pi}{3f_p}\right)^{1/2}\langle r\rangle$, and <*r*> is mean radius of particles. When the obstacles are strong, the interacting dislocations will bow out more, $\hat{\tau} = \frac{0.81f_m}{bL_s}$, and the maximum stress will be $\hat{\tau} = \frac{1.62\Gamma}{bL_s}$ [21]. Furthermore, the precipitates are not monodisperse, so the size distribution of particles should be incorporated (more details in [22]). The mean planar radius is used to replace average radius if the particles are not spherical.

Orowan stress equation, $\tau_{Oro} = \frac{2\Gamma}{bL_s}$, is often used to calculate the stress contribution of non-shearable particles bypassed by dislocations. This equation has been modified in several ways. Ardell [21] gave a modified equation

$$\tau_{Oro} = \frac{1.2732\langle\Gamma\rangle f^{1/2}}{b\langle r\rangle\left(1.1374 - f^{1/2}\right)}, \tag{8}$$

where <Γ> is the geometric mean value of Γ. When the distribution of particles is heterogeneous, the region with fewer obstacles is softer and easier for dislocations to glide through. The regions with high density of obstacles are hard spots, and the critical angle of concave loops is about 90˚. This is called percolation model, more details in [4].

Internal stress

Stress fields in crystals can be either short range, such as with individual dislocations, or long-range internal stresses. The internal stress is manifest in Bauschinger test and cyclic deformation. The build-up of Orowan loops around non-shearable particles

induces strong internal stress compared to grain boundaries. The unrelaxed plastic strain of the particle ε_p can be related to the number of Orowan loops around particles, n, by $\varepsilon_p = \frac{nb}{4r}$, where r is the radius of particles. The internal stress is approximately given by

$$\sigma_b = f_p E_p \varepsilon_p , \quad (9)$$

where f_p is the volume fraction of particles and E_p is the Young's modulus of particles. Brown and Stobbs proposed a framework for the internal stress caused by particles in a series of articles [23-24]. Their work provides detailed discussions on the internal stress.

Work hardening

Several researchers have estimated the athermal work hardening component in stage II due to non-deformable particles from theories (more details in [25]). The work hardening is proposed to be caused by short-range dislocation interactions [26] or long-range elastic internal stress [23-24]. The basic assumption is that crystals containing non-shearable particles are deformed by formation of a set of dislocation loops (Orowan or prismatic loops) around particles which are referred to as geometrically necessary dislocations. The dislocation loops and dipoles around particles have been observed by TEM, and a typical structure was shown in Fig. 2.1.3 [27]. Humphreys and Hirsch also reported that the density of prismatic loops and helices decreased with increasing deformation temperature, and no prismatic loops or helices were found when crystals were deformed at 473K [27].

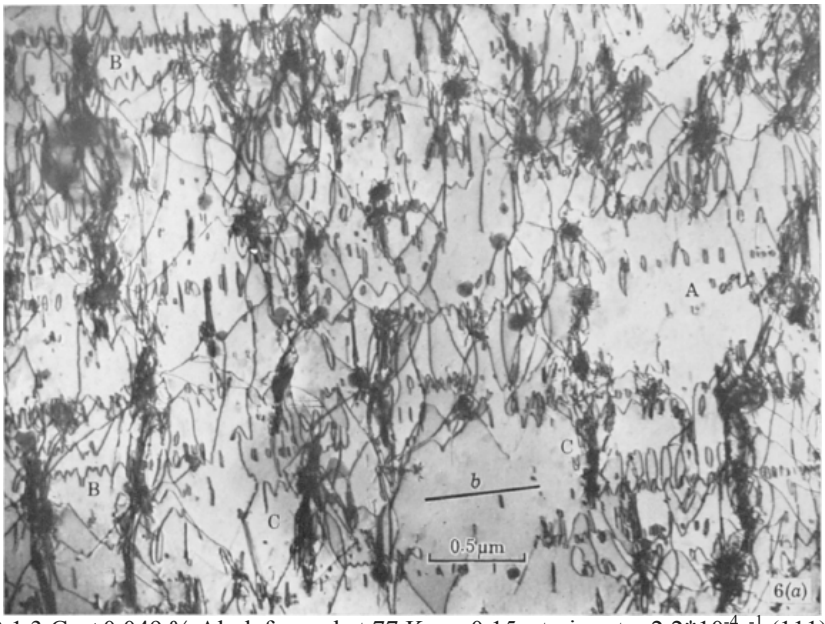

Fig. 2.1.3 Cu +0.049 % Al, deformed at 77 K, ε= 0.15, strain rate=2.2*$10^{-4}s^{-1}$,(111) sections, showing the irregularity of loops (A), the formation of helices (B) and dipole clusters (C).[27]

The athermal hardening component is proportional to the square root of strain, if the stress is relaxed near particles (not Orowan loops but prismatic loops). The equation of stress as a function of strain is different according to different author's assumption, but generally in the form of [25]

$$\tau_p = C\mu\left(\frac{f_p b\varepsilon}{R}\right)^{\frac{1}{2}}, \qquad (10)$$

where f_p is the particle volume fraction, R is the radius and C is a constant. However, this is valid only for low testing temperatures because recovery at higher temperature will make the dislocation loops unstable, leading to invalidity of the basic assumption. Humphreys and Hirsch [27] found that the number of prismatic loops generated at a given strain decreases rapidly with increasing temperature in the range 300-500 K. The particle effect on work hardening at large strains involving dynamic recovery is still unclear.

2.2 Experimental results on the work hardening of alloys

2.2.1 Temperature and concentration dependence of flow stress

Many researchers have studied the flow stress of FCC single crystals at different temperatures, and reported the temperature and concentration dependence of flow stress, particularly based on Cu, Ag and Au (more details in [17]). The critical (resolved) shear stress (CRSS) increases rapidly with decreasing temperature below room temperature for FCC alloys. Between 300 K and 500 K, the critical shear stress shows a nearly temperature-independent "plateau", the height of which increases rapidly with increasing concentration at small solute concentration levels (Fig. 2.2.1-1). It should be noted that the yield stress of single crystals can be determined by different methods from a stress-strain curve. Thus, the values of CRSS vary to some extent by different measurement methods.

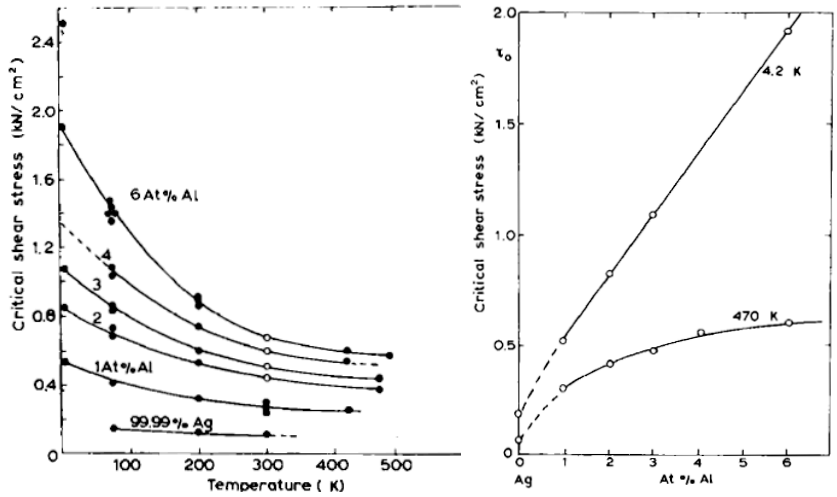

Fig. 2.2.1-1 Critical shear stress (at the strain of about 0.1%) of Ag-Al single crystals versus temperature and solute content [28]

The contribution of solute atoms to flow stress, σ_{ss}, depends on the concentration in a power law. The empirical equation to describe the relation is as followed:

$$\sigma_{ss} = H \cdot c^n, \frac{1}{2} \le n \le 1 \qquad (11)$$

The theory based on the interaction between dislocations and solute atoms predicts n-value could be 1/2 or 2/3, by Friedel statistics and Mott statistics respectively [12].

According to the Labusch parameter, the Fleischer-Friedel theory, $\tau \propto c^{1/2}$ should be valid in very dilute alloys, while Labusch-Mott statistics, $\tau \propto c^{2/3}$, fits the higher concentrated alloys. The experiments on single gold crystals [29] show that most of the results fit $\tau \propto c^{2/3}$, the Labusch theory; only some very dilute (usually <1at%, even ~0.1%) alloys suggested the Friedel theory (Fig. 2.2.1-2). Au-Zn seemed to fit the $\tau \propto c^{1/2}$ law well in relatively high concentration region, but it was difficult to explain in theory. The Labusch theory suggests that Friedel statistics is valid when η is much smaller than 1, which requires a large f_m and large misfit (details in section 2.1.2). However, both the size and modulus misfits of Zn in gold are negative and small. The experiments show that the value of n varies with the concentration, and the transition is difficult to identify. This simple law $\tau \propto c^{2/3}$ is hard to find in polycrystals. The stress exponent of the concentration dependence in polycrystals is from 0.5 to 1 with various strains and temperatures, and this relationship has been found in many alloys [12].

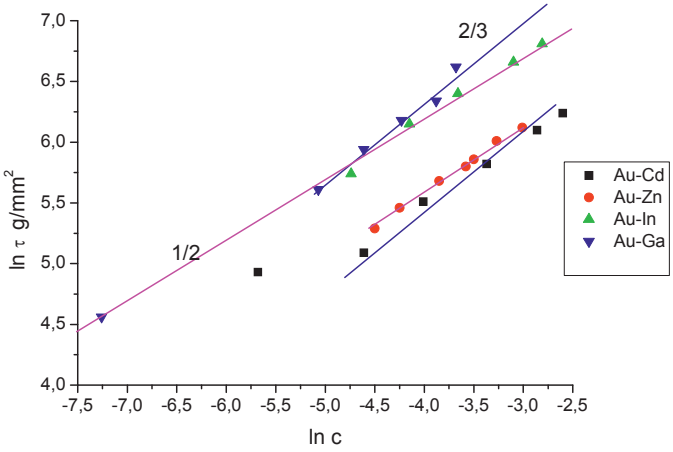

Fig. 2.2.1-2 Plateau stresses of various gold alloys (the slope is labeled) [29]

If the binary solid solution hardening (SSH) of dilute and random distributions of solute atoms i in a base metal is given by $\Delta\tau_i = Hc_i^q$, and no interaction between these distributions is assumed, the total solution hardening is given by:

$$\Delta\tau^{1/q} = \sum \Delta\tau_i^{1/q} . \qquad (12)$$

In Labusch's theory, the value of q is 2/3. This multi-component hardening relation has been found in some ternary single crystals. A good fit of $c^{2/3}$ dependency of the CRSS at 78K in Pb-In-Tl single crystals was shown in Fig. 2.2.1-3 [30], and also in the plateau region of ternary Cu-Si-Ge [31].

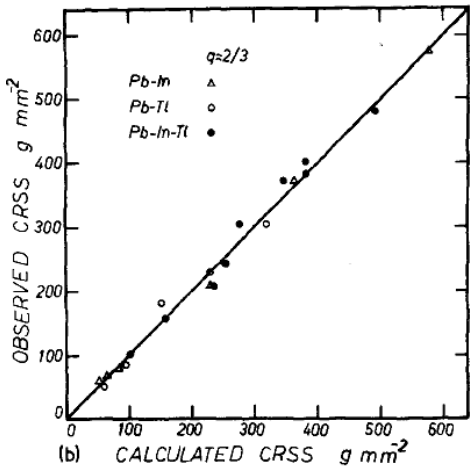

Fig.2.2.1-3 Comparison between observed and calculated critical resolved shear stress of Pb-In-Tl alloys at 78 K [30]

The relationship between flow stress and solute content is also dependent on temperature. The $c^{1/2}$ or $c^{2/3}$ laws which were found to fit the critical shear stress of single FCC crystals between 300K and 500K failed at lower temperatures. For example, the critical shear stress for Ag-Al increases nearly linearly with concentration at 4.2K, which is different from that at 470K (Fig.2.2.1-1). The dependence of the critical resolved shear stress for Ag-In alloys fits the 3/4 and 2/3 power law of the concentration at 300K and 77K respectively [11].

Solid solution hardening is due to certain combination of the size and modulus misfits. Some studies have attempted to find out the relation between solid solution hardening rate and the misfit parameter, which is defined in section 2.1.2 (more details in [12]). Figure 2.2.1-4 shows some results. The Fleischer parameter, $\varepsilon_F = |\eta - \alpha_F \delta|$, appears to

fit the experiments better (less scattered) than Labusch parameter, $\varepsilon_L = \sqrt{\eta^2 + \alpha_L{}^2 \delta^2}$, but it was difficult to explain in theory. The Fleischer parameter was interpreted in terms of the interaction of screw dislocations with solutes and fitted screw dislocations well, while Labusch parameter fitted the edge dislocations well in the Mott-Labusch statistics [13] and the edge dislocations are dominant in FCC alloys. Both these parameters are valid in Labusch's theory, but the theory predictions usually fitted only single crystals, not the experiments for polycrystals. A good universal experimental fitting and explanation are difficult, which is probably due to the variances in the accuracy of parameters, the purity of materials and testing conditions.

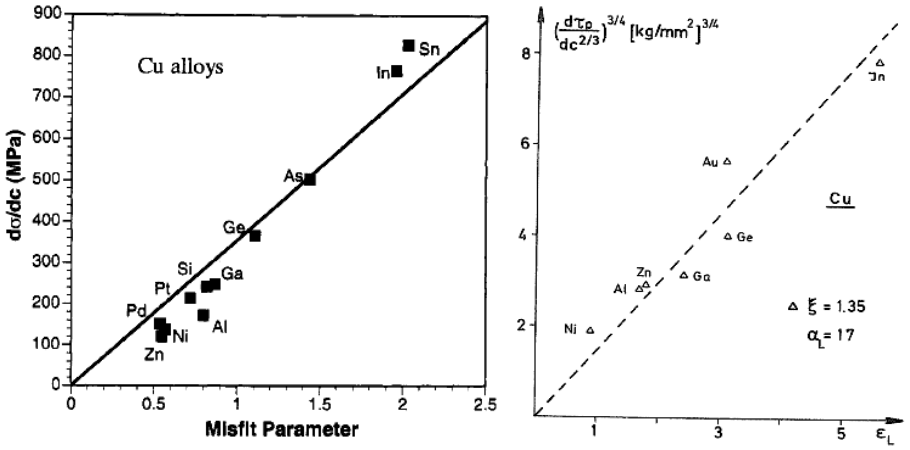

Fig.2.2.1-4 left: the Fleischer plot of solution hardening rate versus misfit parameter (3δ-η) for various copper alloys deformed at 77K [12]; right: solution hardening rate in the plateau region plotted against the Labusch parameter (ξ is second-order parelastic interaction parameter) [17]

Studies on polycrystal alloys also confirm that the value of n in eq. (1) varies with testing temperatures. From the study on Al-Mg and Al-Cu binary alloys [32], from 116K to 650K, in Table 2.2.1 n-value generally decreased with increasing temperatures except 422K (low n and high H at 422K), in a similar trend as the critical shear stress of single crystals. It is necessary to distinguish carefully the concentration dependence in the CRSS-T plateau region and at low temperatures. It is reported [12] that most of the data at the plateau stress for silver, gold, and copper single-crystal alloys fit the $c^{2/3}$ dependence. There are much less CRSS data at low temperatures but there is a plurality in favor of the $c^{1/2}$ dependence. The polycrystal alloys also have a similar trend. The

trend of n-value with temperature in Table 2.2.1 shows a transition at 116K, implying that some change in theoretical assumptions may be needed to explain the n-value at low temperatures. The CRSS-T plateau of Al alloys is usually in 200K-500K, so room and elevated temperatures at which many experiments were carried out are in or above the plateau region. It is noted that n-value and the temperature dependence of n-value varies with solute elements. The values of n in Al-Cu binary alloys are from 1.35 to 0.56, while the values in Al-Mg binary alloys vary from 0.81 to 0.63 in the same temperature region.

Table 2.2.1 Values of the parameters in Eq. (11) for Al-Cu binary alloys at a true strain of 0.05, deduced from [32]

T (K)	78	116	194	293	422	550	650
n	1.07	1.35	0.9	0.75	0.68	0.79	0.56
H (MPa/at%)	78.76	131.98	55.98	69.69	90.49	30.17	9.93

The research on the concentration dependence of flow stress in aluminum polycrystal alloys is usually limited to some binary alloys, like Al-Mg, and more experimental research is required to quantitatively predict the solid solution hardening.

2.2.2 Solute effect on work hardening

The solute content affects the stress-strain curve of alloys, as shown in Fig. 2.2.2-1. The easy glide range and stage II range of alloys become longer compared to pure metals, and stage III starts at higher stresses [14]. The dislocation arrangements in stage II and III of some solid solution alloys, such as Ni-Co and Cu-Al, were observed to be different from those of pure metals. This could be the result of changes in stacking fault energy due to the solute additions [14]. In alloys with unchanged stacking fault energy (like Cu-Mn), dislocation structures at the end of stage I were observed similar as in pure Cu [33].

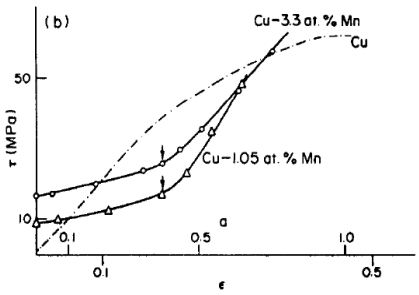

Fig.2.2.2-1 The stress-strain curves of Cu-Mn single crystals compared to pure copper [33]

Hendrickson and Fine [28] calculated the activation volume, V_a, from the measurements of strain rate change tests by the following equation:

$$V_a = \frac{kT \ln\left(\frac{\dot{\varepsilon}_2}{\dot{\varepsilon}_1}\right)}{\tau_2 - \tau_1} \tag{13}$$

The logarithm plot of V_a and solute content in Fig. 2.2.2-2 shows that V_a is proportional to c^{-e}. The value of e was large at low temperature (e=0.82 at 4.2K), and smaller at higher temperature (e=0.65 at 296K). The decrease in V_a with increasing Al content was explained due to an increase in dislocation density. The additions of Al in Ag crystals also refined the subgrains significantly.

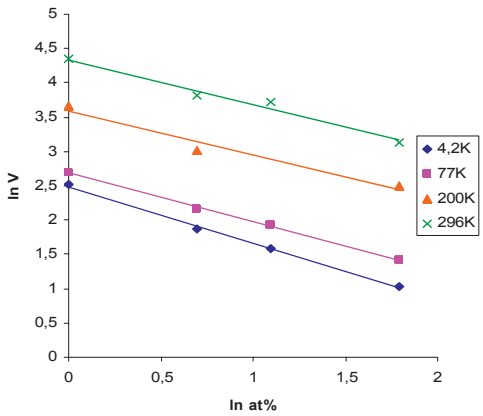

Fig.2.2.2-2 Activation volumes, $V \times 10^{21} \mathrm{cm}^3$, as a function of Al content (values of natural logarithm) and testing temperature [28]

Ryen et al. [34] studied the work hardening of commercially pure Al-Mg alloys. At large strains, stage IV, a low work-hardening rate of high-Mg alloys was observed, and the work-hardening rate in stage IV was almost unaffected by the Mg content (Fig.2.2.2-3). Shear bands tended to form at lower strains as Mg content increases.

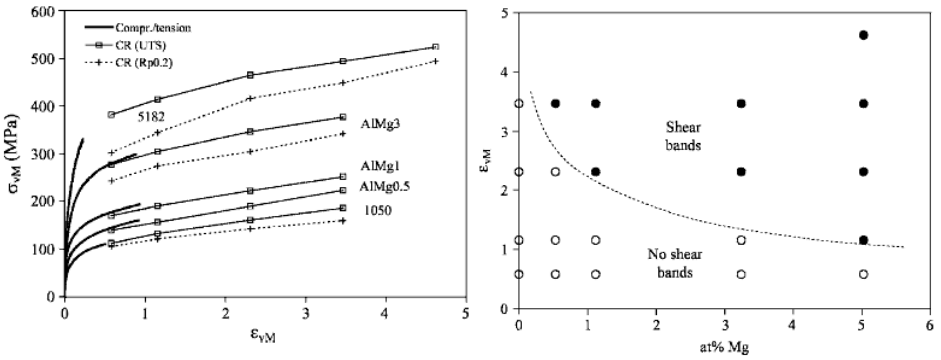

Fig. 2.2.2-3 Left: extended stress-strain curves of Al-Mg alloys. Right: The formation of macroscopic shear bands as a function of cold rolling strain and the concentration of Mg in the alloy. Full circles and open circles represent shear band formation and no shear band formation, respectively. [34]

2.2.3 Influence of impurities

Most of the studies on the concentration dependence of flow stress in early days were on high purity binary alloys. Recent studies on commercial alloys show that solid solution hardening of commercial-purity alloys is stronger than that of high-purity alloys. The n-value of commercial-purity Al-Mg alloys at room temperature is ~1 [35], a bit higher than that of high-purity binary alloys (0.6-0.8) [32]. Ryen's study on Al-Mn alloys also show a similar but smaller difference between high-purity and commercial alloys. In addition, the temperature dependence of n-value in high-purity binary alloys is not seen in commercial alloys, reported in Ryen's PhD thesis. The hot deformation of commercial purity Al-Mg alloys also indicated a similar conclusion [36]. The peak flow stress showed a linear relationship with solute content. This linear relationship is insensitive to Zener-Hollomon parameter in the hot-deformation regime. However, the original torsion and compression data of Al-Mg alloys by Rønning [36] only had three solute levels, which was not enough for good statistics to make a convincing conclusion.

The impurity level also affects the grain size dependence of strength, i.e. the Hall-Patch relation. Hansen [37] reported that the value of k in $kd^{-1/2}$ in high-purity (99.999%) aluminum was almost twice as that in 99.5% commercially pure aluminum. The concentration dependence of flow stress in commercial-purity binary alloys is different from that of high-purity binary alloys, implying that impurities affect the flow stress. The hot compression data provided in [38] showed that impurity level in high-purity aluminum also affected the flow stress significantly. The flow stress increased with increasing impurity level (Fig.2.2.3). This impurity impact was stronger at low temperature or high strain rate, i.e. at a higher Zener-Hollomon parameter.

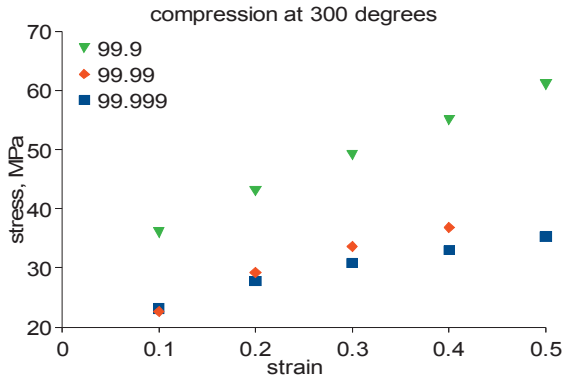

Fig.2.2.3 Various levels of high purity (99.9%, 99.99% and 99.999%) aluminum compressed at 300ºC at a strain rate of $0.1s^{-1}$. [38]

The impurities in commercial alloys, including mainly Fe and Si are usually above 0.1wt%, and affect the flow stress significantly. But the comparison of experimental results from different sources needs more consideration, because the thermo-mechanical histories are different, resulting in differences in the grain size and textures, and sometimes particles, each of which also affects the flow stress. Few quantitative studies on the effect of impurities on work hardening are reported, since the impurity content is difficult to control.

2.2.4 Influence of dispersoids or precipitates

Alloying elements may form constituent particles or precipitates during casting or the following heat treatments. These dispersed particles can strengthen the materials by

precipitation hardening. Many studies show that work hardening of heat-treatable aluminum alloys varies under underaged, peakaged and overaged conditions [39-40]. It is reported that at peak strength, the work hardening is minimum (Fig.2.2.4-1) [40]. As the yield stress increases from the natural aging (NA) to the peak aging (PA) condition, the work-hardening rate decreases to a minimum at peak aging condition. This is due to the depletion of solute atoms in the solid solution and the presence of shearable particles in the under aging and peak aging condition. In the over aging (OA) condition, the work hardening rate increases again as the dislocations accumulate due to non-shearable particles.

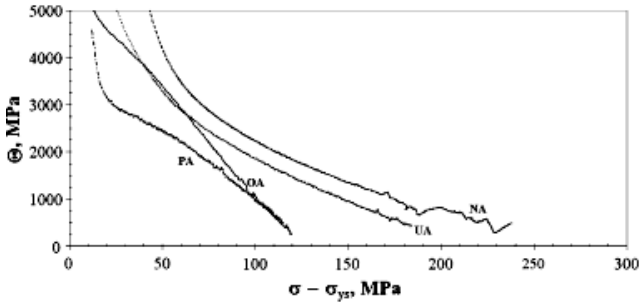

Fig.2.2.4-1 Kocks-Mecking plots for AA2219 in four aging conditions (natural aging, under aging, peak aging and over aging) [40]

Deschamps et al. [41] studied the influence of precipitation on strain hardening through Kocks-Mecking plots in Al-Zn-Mg and Al-Mg-Si-Cu. They found that shearable precipitates do not seem to influence greatly the work hardening behavior, which is then mostly controlled by the solute content. Non-shearable precipitates induce a high initial hardening rate, but this high initial value cannot be sustained to high strains due to extensive dynamic recovery in the solute-depleted matrix. Study on the flow stress of underaged, peakaged and overaged samples of the γ′-hardened Ni based superalloy Inconel X-750 [42] showed some evidence on the influence of particles on the strain rate sensitivity. It was found that a progressive increase of strain rate sensitivity parameter *m*, indicated by the slope in the Haasen plot, during Stage II of work hardening, was correlated with the increase in the γ′-precipitate size with a constant precipitate volume fraction.

Non-shearable particles

The presence of strong, non-deformable particles in alloys results in considerable inhomogeneous distribution of strain and dislocations, and hence the work hardening should be different from alloys containing weak and shearable particles. Hirsch and Humphreys [43] have studied the influence of non-deformable particles on stress and microstructure of single crystals of Cu. Figure 2.2.4-2 shows the initial region of work hardening with low hardening rate at 77K, before the work hardening becomes parabolic. The slope of the curves should be proportional to $(f_p/R)^{1/2}$, according to Eq. (10) (refer to section 2.1.3). The slopes of experimental τ-$\varepsilon^{1/2}$ curves at 77K had a good linearity with $(f_p/R)^{1/2}$ within low hardening rate region, but the results at 293K did not fit as well as those at 77K.

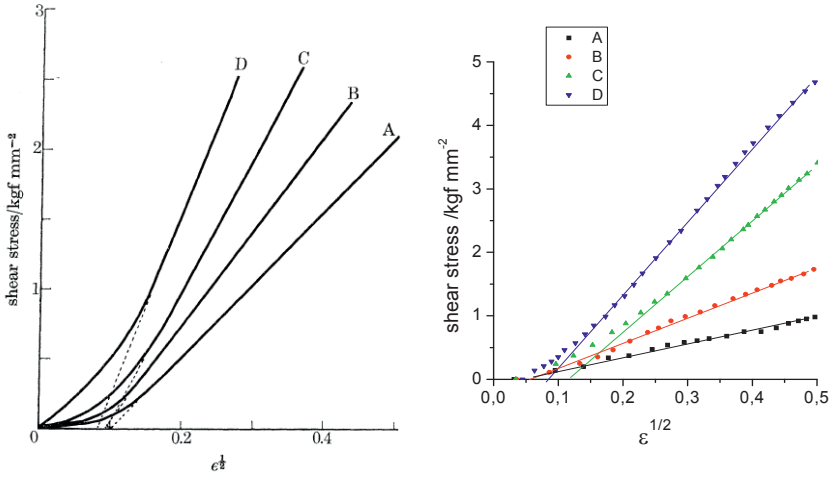

Fig.2.2.4-2 The work hardening (τ-τ_0) of copper single crystals containing various amounts of Al_2O_3 particles (sizes and volume fractions listed in the table below) at 77 K(left) and 293K (right)(strain rate=$2.2\times10^{-4}s^{-1}$) [43].

	A	B	C	D
Volume fraction $f/10^{-3}$	1.13	2.2	4.5	8.8
effective radius on a slip plane /nm	22	25	33.5	39

The work-hardening of dispersion-hardened alloys decreased rapidly with increasing deformation temperature around room temperature (summarized in [44]). This temperature dependence was ascribed to dynamic recovery or relaxation of Orowan loops by climb through the pipe diffusion. Matsuura [44] calculated the distribution of

Orowan loops and the calculation well explained the temperature dependence of work-hardening qualitatively.

The study on aluminum containing nano-size alumina particles [45] confirmed the parabolic work-hardening at small strains. Moreover, the stress-strain curves of the dispersed alloys were practically parallel to the curve of 99.5% pure aluminum at large strain (>3%). The work-hardening rate increased with increasing volume fraction of particles and decreasing particle size (decreasing particle spacing). Hansen and Bay [46] found that neither the content nor the distribution of fine dispersed particles (0.6-1.2 wt% Al_2O_3, D=46nm) in Al affected subgrain size significantly after 50-90% drawing, even if the particle spacing (170nm) was much smaller than the subgrain size (290nm), while the subgrain sizes of Al containing particles were smaller than that of pure Al. However, after cold drawing, the increase in hardness of the alloy containing low density of dispersed particles was slightly higher than that of containing high density of particles, no mater the particles dispersed uniformly or in the network. This implies that dispersoids affected work hardening little at large strains. Barlow and Hansen [47] found that at small strains, the subgrain sizes in different regions were rather different, with smaller subgrains in the areas with higher concentrations of alumina particles. Barlow et al [48] investigated the evolution of subgrains, misorientations and textures of Al containing 3.8vol% alumina during cold-rolling. The fraction of high-angle boundaries, which was already very high (59%) at a strain of 1.4, continued to increase with rolling strain (72% at a strain of 3.5).

The non-deformable particles generally increase the initial work-hardening rate. This effect of non-deformable particles was also confirmed by iron rich constituent particles (1-5μm), and this effect became weaker as strain increased, as shown in Fig. 2.2.4-3 [49]. Dowling and Martin [50] also found that α-$Al_{12}Mn_3Si$ dispersoids in Al-Mg-Si alloys reduced the slip band spacing at small strain and the spacing decreased progressively with strain, which indicated that the dispersoids homogenized the slip distribution.

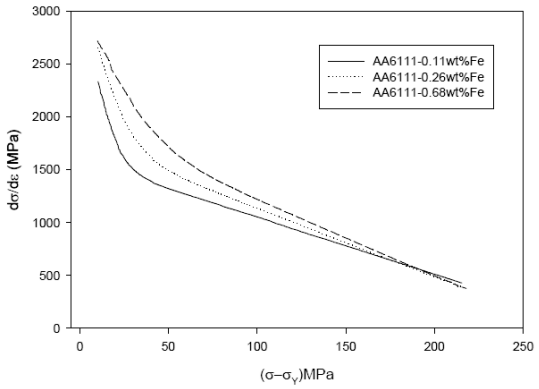

Fig.2.2.4-3 Work hardening rate for AA6111 in T4 temper (i.e. natural aged) illustrating the effect of volume fraction (implied by Fe content) of large particles [49].

Most of the studies on the influence of precipitates on work hardening focus on heat-treatable alloys, because the small precipitates have a high number density, and contribute significantly to the strength. In non-heat-treatable alloys, little attention is paid to those fewer and relatively larger particles. Moreover, the studies on precipitation hardening and particle reinforced composites focused on the yield stress and the flow stress at small strain. It is reported that the hardness and 0.2% yield stress of Al-3.8% alumina decreased a little at large strains [48]. However, few studies report the influence of particle distribution on flow stress at moderate and large strain.

2.2.5 Al alloys containing Mn, Fe or Si

Recently ab-initio calculations were performed to estimate the solute-dislocation interactions in aluminum. The first-principles studies [51-52] suggest that the solute strengthening effect of Fe or Mn is among the strongest, Mg intermediate, and Si among the weakest. These predictions should be quantitatively compared to the experimental results. Ryen et al. [35] studied the solid solution hardening of both commercial and high purity Al-Mn alloys. The solute strengthening rate was about 50 to 60% stronger in the commercial alloy compared to the high-purity material. This strong Mn effect in commercial alloys was considered to be attributed to a synergy effect between Mn and trace elements in solid solution. Nearly linear trend lines fitted best for both the commercial and the high-purity alloys (Fig.2.2.5-1). However, better statistics in terms

of more data points for the high-purity Al-Mn would be required to make convincing conclusions.

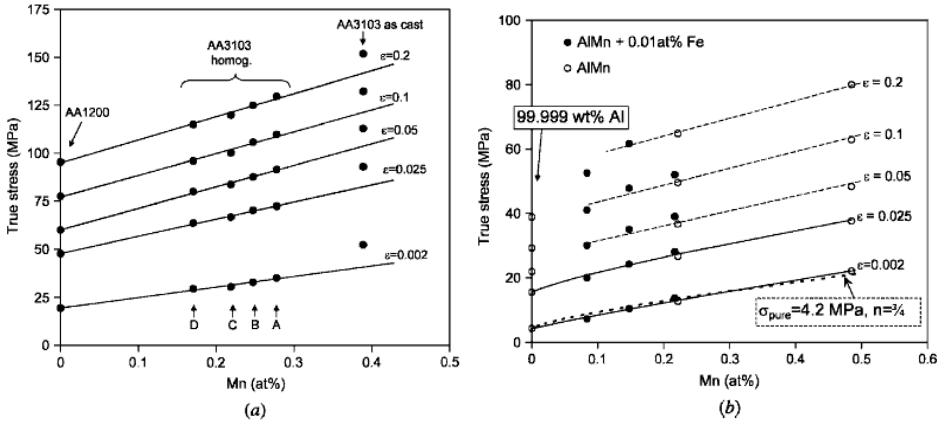

Fig. 2.2.5-1 Flow stress at various strain levels as a function of the amount of Mn in solid solution (at.%) (a) for the various conditions of the AA3103 alloy and (b) for high-purity Al-Mn alloys [35]

Solute atoms may interact with vacancies. Wolverton [53] calculated the solute-vacancy binding energy using the plane wave pseudopotential method. The calculated binding energies suggest that Si atoms attract vacancies most at the first nearest neighbors, while Mn and Fe atoms attract vacancies only at the second nearest neighbors. The preferable Si-vacancy binding is also suggested by other first-principle calculations [54].

Solute atoms may interact with each other, i.e. forming clusters as pinning obstacles. Kosugi and Kino [55] measured the binding free energy between a dislocation and a pinning obstacle in Al-Si single crystal and 99.999% Al by amplitude-dependent internal friction method. The binding energy at low temperature (2-14K) was 0.05-0.06eV and 0.5-0.8eV for 99.999% Al and Al-0.01at%Si, respectively. The value of binding energy in Al-Si was too large for a dislocation- solute atom interaction because the binding energy in 99.9999% Al+ 1ppm Si was determined to be 0.12eV at room temperature, which should be a dislocation-solute atom interaction. Furthermore, the binding energy in Al-Si increased after natural aging. It was concluded that the measurement results could be interpreted as dislocation-cluster interaction. Kosugi later [56] determined the interaction energy for other dilute (20-100ppm) Al alloys. The

interaction energies were determined as 0.11, 0.12, 0.135, 0.19 and 0.195eV for Zn, Li, Ag, Mg and Cu solute atoms, respectively. Furthermore, it was found that at relatively low temperatures (or high stress amplitude), the decrease of the stress with increasing temperature was proportional to $T^{2/3}$ down to 65% of the stress for 0 K, and then deviates from the $T^{2/3}$ dependence. The elementary process was explained as unpinning of a dislocation from a single solute atom. At relatively high temperatures (or stress less than 40% of that for 0 K), the stress changed as proportional to T^{-1} for all dilute Al alloys but for a pure Al crystal. The elementary process was explained as simultaneous unpinning of a dislocation from several solute atoms for dilute alloys.

Some studies on non-heat-treatable alloys have shown that the constituent particles or dispersoids in non-heat-treatable alloys, like 3xxx alloys, affected the flow stress and work hardening. Figure 2.2.5-2 shows the influence of dispersoids on work hardening in AA3207 alloys [57]. After cold rolling, annealing for 30000 seconds at 350℃ and recrystallization, dispersoids precipitated. The work hardening rate of this sample (curve 2 in Fig. 2.2.5-2) was higher than that of solid solution alloys (curve 1 in Fig. 2.2.5-2) for small strains, but lowers at high strains, and the curves eventually crossed each other.

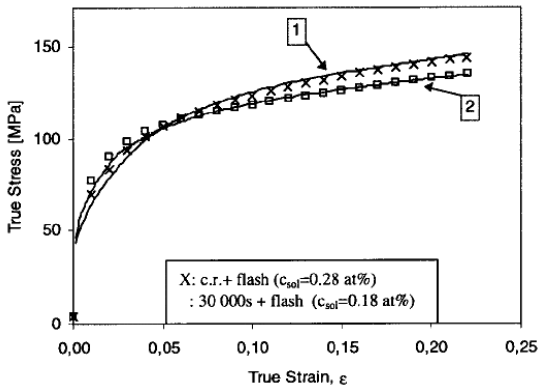

Fig. 2.2.5-2 The stress-strain curves of AA3207 alloys.1) no dispersoids, 2) with dispersoids [57].

Chinh et al [58] studied the effect of Fe and Si on high temperature strain rate sensitivity of as cast Al-Mn. The high temperature strain rate sensitivity between Al-Mn

and Al-Mn-Fe-(Si) was different, while Al-Mn-Fe and Al-Mn-Fe-Si behaved similarly. However, it was difficult to interpret because the addition of Fe and Si introduced new phase precipitates and reduced the amount of AlMn particles. No quantitative measurements of particles were done to clarify the mechanical phenomena.

The misfit volume of Si in Al is small (-2.6 A^3) and thus Si in solution contributes weakly to the strength compared to Mg or Cu, according to theoretical prediction [52]. Studies on the mechanical properties of hypo/hyper-eutectic Al–Si alloys [59] show that hardness, Young's modulus and also brittleness increased with Si content.

In fact, the solubility of most alloying elements in aluminum is low except for Mg. For example, most of Mn, Fe and Si are not in solid solution, but form particles i.e. $Al_6(Mn,Fe)$ and α-$Al_{12}(Mn,Fe)_3Si$ [60-61]. These particles, particularly the fine dispersoids, affect the work hardening, but the influence is unclear because most of the research on particle impact is carried out by comparing the work hardening during aging treatment, while solute content changes as well. Few quantitative studies have been reported in this aspect.

2.3 Microstructure of Al-(Mn)-Fe-Si alloys

2.3.1 Al-Fe-Si

The equilibrium solubility of Fe in Al is very low, about 0.05wt% at eutectic temperature, and decreases quickly with decreasing temperature, as shown in Fig. 2.3.1 [62]. Most of Fe atoms exist in the form of constituent particles, which form during casting and homogenization. The Fe content and solidification cooling rate influence the types of constituent particles (intermediate phases). The composition of Al_xFe might vary from Al_3Fe to Al_6Fe [63]. In commercial alloys, the impurity Si also affects the constituent particles of Fe. In dilute Al-Fe-Si alloys, α- and β-AlFeSi forms besides θ-Al_3Fe and Al_6Fe during homogenization. It is reported that β-AlFeSi is more likely to form in alloys with low Fe/Si ratio [64].

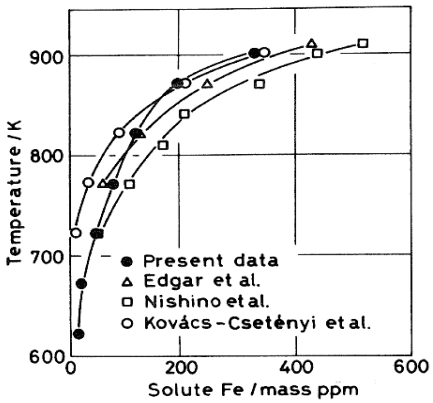

Fig. 2.3.1 The solubility of Fe in Al [62].

2.3.2 Al-Mn-Fe-Si

In 99.99% pure Al-Mn alloys, a phase transition was observed in the precipitation process at about 550°C [65]. It was supposed that above this critical temperature Al_6Mn particles were formed, while below this temperature $Al_{12}Mn$ particles were formed in the as-cast alloy. The addition of Fe significantly accelerated the precipitation process, i.e. Fe favors the precipitation of $Al_6(Mn,Fe)$. No transition phenomena seemed to occur in Al-Mn-Fe-Si. This is reasonable since additional α-Al(Mn,Fe)Si particles are formed in alloys containing Si both by interdendritic precipitation during solidification and by heterogeneous nucleation and growth in supersaturated grains when the alloy is annealed. In commercial 3xxx alloys, cubic type α-Al(Mn,Fe)Si and orthorhombic type $Al_6(Mn,Fe)$ are the two main types of dispersoids.

The Mn/Fe ratio in dispersoids and primary particles changes during heating. The Mn/Fe ratio of the primary particles increased from 0.57 in the as-cast state to 0.59 after heating to 600 °C, and increased to 0.79 after 7 h of homogenization at 600 °C [61]. It is found that some primary particles $Al_6(Mn,Fe)$ transform into α-AlMnFeSi phase during heat treatment. The transition speeds up at 400°C and the fraction of α-AlMnFeSi in total constituent particles is around 30% at 600°C [61]. At low temperatures, the precipitation of dispersoids is controlled predominantly by nucleation and growth. The size evolution of primary particles below 560°C is controlled mainly by breaking up. As temperature increases, coarsening becomes the predominant mechanism to control the

size evolution, which results in spheroidization of the primary particles and the decrease of number density and the increase of dispersoid size [60-61]. During the solidification, a strong manganese depletion forms on the periphery of dendrite arms. Precipitate free zones (PFZ) are formed around primary particles, and the evolution is shown in Fig. 2.3.2-1. At high temperatures (above 500°C), the primary particles begin to coarsen [61] and cause the dispersoids around them to dissolve, leading to a larger PFZ [60].

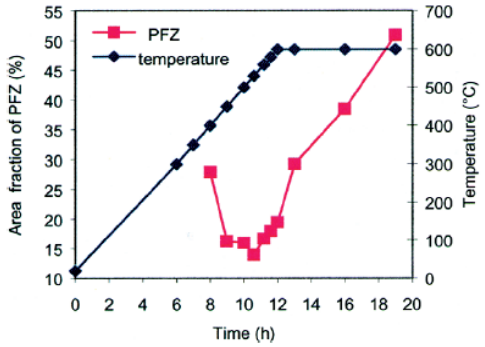

Fig. 2.3.2-1 The evolution of PFZ during heating and homogenization. [60].

Effect of Si

It is reported [66] that Si did not have a strong influence on the as-cast solute level of Mn in 3xxx alloys, indicated by the electrical conductivity measurements; and Si promoted the precipitation and growth of α-Al(Mn,Fe)Si during the heating-up part of homogenization. The fraction of α-Al(Mn,Fe)Si in the constituent particles increased significantly with addition of Si in as-cast alloys as shown in Fig. 2.3.2-2.

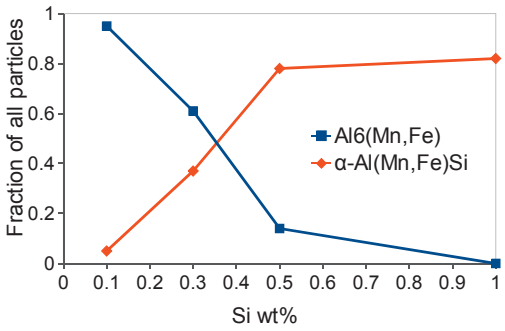

Fig. 2.3.2-2 The fraction of α-Al(Mn,Fe)Si and Al_6(Mn,Fe) in total primary particles in as-cast Al-1Mn-0.5Fe-(0.1-1.0)Si alloys (Si particles appeared in alloys containing high Si content, like 1wt%) from [66].

Chapter 3 Experimental techniques

3.1 Mechanical testing

Mechanical testing provides information about the mechanical properties of materials, such as strength, ductility and work hardening behavior. In this section, a brief description of the methods used in present work is given in the following text. General introductions of mechanical testing have been presented in many textbooks of materials science and engineering, e.g. *Mechanical Metallurgy* by Dieter. Detailed description of test methods could be found in relevant ASTM standards or *ASM Handbook, Volume 8 - Mechanical Testing and Evaluation*.

Tensile tests

Tensile test is a standard technique to measure the mechanical properties of materials. Stress-strain curves are measured from tensile tests. The procedure of measurements is referred to ASTM E8M-09. In present work the tests were performed at room temperature. The strain rate was in the range of 10^{-4} -$10^{-1}s^{-1}$. The gauge length was 25 or 10 mm. The 0.2% proof yield strength, ultimate tensile strength and uniform elongation can be determined by tensile tests.

Vickers hardness tests

Vickers hardness test is a simple method to measure micro-hardness, requiring less effort and materials than tensile tests. Hardness can be used to estimate the strength of materials, but it is not directly scaled with yield strength or tensile strength. A method of estimation of yield strength from hardness was proposed in [67]. In present work, a load of 500 g was applied for 15 seconds.

3.2 Structure characterization

Materials science investigates the relationship between the processing, the structure and the properties. The structure encompasses atomic arrangements, chemical structure and grain-scale microstructure. The following instruments were used to characterize structure.

Optical microscopy

For anisotropic crystals, grains of different orientations have different values of polarized light reflectivity. Then polarized light microscopy could be used to characterize the grain structure. However, aluminum has a cubic crystal structure, and is not sensitive to the polarization. Thus a layer of anisotropic coating on the surface is required to reflect polarized light. Anodized aluminum surface displays contrast under polarized light. Anodization instrument is the same as electropolishing. Samples are connected to the anode. Anodization is performed at room temperature, at a voltage of 20-30 V for 2 min, using 1% HBF_4 solution.

Scanning electron microscopy

Scanning electron microscope (SEM) is used for microstructure observation. The most common mode uses secondary electron detector, which is generally for the morphology of sample surface. Heavy elements reflect more backscattered electrons (BSE), so the BSE images can show chemical composition contrast. BSE imaging was used for observation of particles containing more Fe and Mn.

Electron back-scatter diffraction (EBSD) technique is used for crystalline materials to characterize grain orientation, boundary misorientation and texture. Zeiss Supra/Ultra 55 with EBSD detector was used in this work, and the results of EBSD were analyzed by TSL software.

Electron probe microanalyzer (EPMA) is fundamentally the same as an SEM, with the added capability of chemical analysis. It can quantitatively measure chemical composition at micro-scale by wavelength-dispersive spectroscopy (WDS). WDS has a much better energy resolution than energy dispersive spectroscopy (EDS), and its detection limit is ~0.01-0.002 wt% [68]. JEOL JXA-8500F was used to measure chemical composition in the present work.

Transmission electron microscopy

Transmission electron microscopy (TEM) is a useful technique to characterize nano-scale microstructure, e.g. fine particles or dislocations. JEOL-2010 was used in the present work. Thin foils for TEM were ground to ～100 μm, and double jet polished with a 1/3 nitric acid methanol solution, at -20 ºC and 20 V.

Chapter 4 Summary and remarks

4.1 Summary

The present work involves several topics: the influence of dispersoids on work hardening, solid solution hardening of aluminum alloys and multi-component hardening. The results are presented in the following articles.

Article 1&2

An Al-Mn-Fe-Si model alloy was used to investigate the influence of dispersoids on work hardening. This model alloy had similar composition as commercial AA3103 alloy. After homogenization, the alloy contains fine dispersoids, coarse constituent particles and solutes in solid solution. Therefore, this alloy provides a complex system to study, which is of academic and industrial interest. Article 1 is the experimental investigation of the dispersoid effect. In order to reduce microstructure variable, well-designed homogenization treatments were carried out to achieve similar solute content of the samples for comparison. The work hardening behavior of as-homogenized and cold-rolled alloy was tested by tension at room temperature. The corresponding microstructure was characterized by TEM and SEM. The strengthening mechanisms during deformation were discussed, including Orowan stress, internal stress and forest hardening. It is found that a high density of fine dispersoids strengthens the alloy significantly, but their effect diminishes as strain increases.

After the experimental investigation of the effect of dispersoids, it was attempted to capture their effect by a model. Modeling of the work hardening is based on either dislocations from the view of microstructure or phenomenological models (e.g. Voce equation). It is challenging to model a complex system such as the alloy in present work, since quantitative modeling of work hardening in solid solution alloy still needs further development. The classical Kocks-Mecking model was used in article 2. A simplified model of dislocation evolution caused by dispersoids was proposed.

Article 3&4&5

Solid solution hardening has been investigated for decades, but the mechanism in a multi-component solid solution has not been fully clarified. Commercial aluminum alloys usually contain several alloying elements besides trace elements. The effect of each element and the interaction between these elements are not yet well understood. The effect of alloying elements and trace elements on strengthening is the topic of the following articles.

In article 3, the effect of trace elements on the strengthening of commercially pure aluminum is investigated. A high-purity base aluminum with addition of Si and Fe was compared to a commercial-purity aluminum containing similar content of Si and Fe. Their mechanical properties were similar, suggesting that trace elements play a minor role in strengthening.

In article 4, solid solution hardening of Al-Si alloys of commercial purity was investigated by tensile testing several Al-Si alloys at room temperature. The effect of Si on strengthening and work hardening was quantitatively characterized. Quenching is found to affect the solution hardening at small strains.

After study on solute strengthening of binary alloys, solute strengthening of alloys containing several elements can be studied. In article 5, the multi-component hardening is investigated by comparison of Al-Mn-Si ternary alloy and Al-Mn binary alloys. The high purity base metal was used in this work, because particles exist in commercial purity base metals and they are difficult to eliminate. The superposition is usually applied under the assumption of no interaction between elements. However, experimental results suggest that this simple superposition can not explain the hardening in the ternary alloy. Clustering is assumed to cause the hardening of the ternary alloy.

4.2 Suggestions for future work

1. Modeling of work hardening incorporated geometrically necessary dislocations is attempted at small strains in the present work. Next step of work may be to extend it to larger strains, and then one parameter approach of Kocks-Mecking might be replaced by

other models. The solute effect on internal stress is not considered in this work, but it is important for industrial applications.

2. In article 4, solid solution hardening of water quenched Al-Si alloys is found to be different from that of air cooled Al-Si at small strains (<0.01). This phenomenon disappeared at larger strains. This implies that Si atoms interact with quenched-in vacancies or other defects due to quenching. The ab-initio calculations suggest that Si-vacancy binding is preferable. However, the interaction mechanism is not yet clarified by experiments. High resolution TEM and positron annihilation lifetime spectroscopy may be useful for the research. The effects of quenching speed and ageing also needs to be studied to understand the mechanism.

3. It may be interesting to compare the strength of high-purity Al-Fe and Al-Si binary alloys to Al-Fe-Si ternary alloy fabricated from the same base metal. It could help to clarify the multi-component hardening in article 3&5.

References

[1] Fuglestvedt J, Berntsen T, Myhre G, Rypdal K, Skeie RB. Proceedings of the National Academy of Sciences of the United States of America 2008;105:454.
[2] Argon AS. Mechanical properties of single-phase crystalline media: deformation at low temperatures, in: Cahn RW, Haasen P, editors. Physical metallurgy, vol. 3. Amsterdam: North-Holland; 1996.
[3] Nes E. Prog. Mater. Sci. 1997;41:129.
[4] Kocks UF, Mecking H. Prog. Mater. Sci. 2003;48:171.
[5] Kocks UF. Journal of Engineering Materials and Technology, Transactions of the ASME 1976;98 Ser H:76.
[6] Estrin Y, Mecking H. Acta Metall. 1984;32:57.
[7] Kuhlmann-Wilsdorf D. Metallurgical Transactions 1970;1:3173.
[8] Kuhlmann-Wilsdorf D. Mater. Sci. Eng., A 1989;113:1.
[9] Nes E, Marthinsen K. Mater. Sci. Eng., A 2002;322:176.
[10] Nes E, Marthinsen K, Brechet Y. Scr. Mater. 2002;47:607.
[11] Hammar RH, Yeh WCT, Oakwood TG, Hendrickson AA. AIME MET SOC TRANS 1967;239:1693.
[12] Mitchell TE. Yielding in crystals containing atomic-size obstacles, in: K.H. Jürgen Buschow RWC, et al, editor. Encyclopedia of materials : science and technology. Amsterdam: Elsevier; 2001.
[13] Neuhäuser H, Schwink C. Solid solution strengthening, in: Cahn RW, Haasen P, Kramer EJ, editors. Materials Science and Technology: a comprehensive treatment. Weinheim: Wiley-VCH; 2005.
[14] Haasen P. Mechanical properties of solid solutions, in: Cahn RW, Haasen P, editors. Physical Metallurgy (Fourth Edition). Oxford: North-Holland; 1996.
[15] Schwarz RB, Labusch R. Journal of Applied Physics 1978;49:5174.
[16] Messerschmidt U. Dislocation Dynamics During Plastic Deformation. Berlin, Heidelberg: Springer-Verlag Berlin Heidelberg, 2010.
[17] Haasen P. Solution hardening in fcc metals, in: Nabarro FRN, editor. Dislocations in Solids. New York: North-Holland; 1979.
[18] Argon AS. Strengthening Mechanisms in Crystal Plasticity: Oxford University Press, 2007.
[19] Leyson GPM, Hector Jr. LG, Curtin WA. Acta Mater. 2012;60:3873.
[20] Ardell AJ. Metall. Trans. A 1985;16:2131.
[21] Ardell AJ. Yielding in crystals containing finite dispersed obstacles, in: Buschow KHJ, R.W. Cahn ea, editors. Encyclopedia of materials : science and technology. Amsterdam: Elsevier; 2001.
[22] Nembach E. Particle strengthening of metals and alloys. New York: Wiley, 1997.
[23] Brown LM, Stobbs WM. Phil. Mag. 1971;23:1185.
[24] Brown LM, Stobbs WM. Phil. Mag. 1971;23:1201.
[25] Gerold V. Precipitation hardening, in: Nabarro FRN, editor. Dislocations in solids, vol. 4. New York: North-Holland; 1979.
[26] Ashby MF. Phil. Mag. 1970;21:399.
[27] Humphreys F, Hirsch P. Proc. R. Soc. London, A 1970;318:73.

[28] Hendrickson AA, Fine ME. Trans AIME 1961;221:967.
[29] Jax P, Kratochvil P, Haasen P. Acta Metall. 1970;18:237.
[30] Gypen LA, Deruyttere A. J. Mater. Sci. 1977;12:1034.
[31] Friedrichs J, Haasen P. Phil. Mag. 1975;31:863.
[32] Sherby OD, Anderson RA, Dorn JE. J. Metals 1951;3:643.
[33] Steffens T, Schwink C. Acta Metall. 1983;31:2013.
[34] Ryen Ø, Laukli HI, Holmedal B, Nes E. Metall. Mater. Trans. A 2006;37:2007.
[35] Ryen Ø, Nijs O, Sjölander E, Holmedal B, Ekström HE, Nes E. Metall. Mater. Trans. A 2006;37:1999.
[36] Rønning B, Nord-Varhaug K, Furu T, Nes E. Mater. Sci. Forum 2000;331:571.
[37] Hansen N. Acta Metall. 1977;25:863.
[38] Prasad Y, Sasidhara S. Hot working guide: a compendium of processing maps. Materials Park, OH: ASM International, 1997.
[39] da Costa Teixeira J, Bourgeois L, Sinclair CW, Hutchinson CR. Acta Mater. 2009;57:6075.
[40] Sharma VMJ, Sree Kumar K, Nageswara Rao B, Pathak SD. Metallurgical and Materials Transactions A 2009;40:3186.
[41] Deschamps A, Esmaeili S, Poole WJ, Militzer M. Journal De Physique. IV : JP 2000;10:151.
[42] Del Valle JA, Picasso AC, Romero R. Acta Mater. 2003;51:6443.
[43] Hirsch P, Humphreys F. Proc. R. Soc. London, A 1970;318:45.
[44] Matsuura K. Acta Metall. 1981;29:643.
[45] Hansen N. Acta Metall. 1970;18:137.
[46] Hansen N, Bay B. J. Mater. Sci. 1972;7:1351.
[47] Barlow CY, Hansen N. Acta Metall. 1989;37:1313.
[48] Barlow CY, Hansen N, Liu YL. Acta Mater. 2002;50:171.
[49] Embury JD, Poole WJ, Lloyd DJ. Mater. Sci. Forum 2006;519-521:71.
[50] Dowling JM, Martin JW. Acta Metall. 1976;24:1147.
[51] Vannarat S, Sluiter M, Kawazoe Y. Physical Review B 2001;64:224203.
[52] Leyson GPM, Curtin WA, Hector LG, Woodward CF. Nat. Mater. 2010;9:750.
[53] Wolverton C. Acta Mater. 2007;55:5867.
[54] Hirosawa S, Nakamura F, Sato T. Mater. Sci. Forum 2007;561-565:283.
[55] Kosugi T, Kino T. Journal of the Physical Society of Japan 1984;53:3837.
[56] Toshio K. Mater. Sci. Eng., A 2001;309–310:203.
[57] Forbord B, Marthinsen K, Nes E. Mater. Sci. Forum 2000;331-337:557.
[58] Chinh NQ, Rajkovits Z, Vörös G, Kovács I. Key Engineering Materials 1991;44:257.
[59] Gupta M, Ling S. Journal of Alloys and Compounds 1999;287:284.
[60] Li YJ, Arnberg L. Acta Mater. 2003;51:3415.
[61] Li YJ, Arnberg L. Mater. Sci. Eng., A 2003;347:130.
[62] Komatsu S, Ikeda M, Muramatsu T, Matsuo M. Key Engineering Materials 1991;44:31.
[63] Griger A, Stefániay V, Kovács-Cseténvi E, Turmezey T. Key Engineering Materials 1991;44:17.
[64] Turmezey T, Stefániay V, Griger A. Key Engineering Materials 1991;44:57.
[65] Vörös G, Kovács I. Key Engineering Materials 1991;44:247.
[66] Pettersen T, Li YJ, Furu T, Marthinsen K. Mater. Sci. Forum 2007;558-559:301.

[67] Cahoon J, Broughton W. Metallurgical Transactions 1971;2:1971.
[68] Kuisma-Kursula P. X-Ray Spectrometry 2000;29:111.

Articles

Article 1

Influence of dispersoids on microstructure evolution and work hardening of aluminum alloys during tension and cold rolling

Qinglong Zhao[a], Bjørn Holmedal[a], Yanjun Li[b]

[a] Department of Materials Science and Engineering, Norwegian University of Science and Technology, Trondheim N-7491, Norway

[b] SINTEF Materials and Chemistry, Trondheim N-7465, Norway

Abstract: The influence of dispersoids on work hardening of aluminum during tension and cold rolling has been studied by comparing Al-Mn alloys containing similar amounts of solutes but various dispersoid densities. The microstructure evolution with deformation strain was examined in transmission and scanning electron microscopy. It is found that a high density of fine dispersoids strengthens the materials significantly, but their strengthening effect diminishes as the strain increases. From a series of Bauschinger tests, it is found that the internal stress due to particles increases rapidly at the initial stage of deformation, but saturates at strains larger than 5%. It is concluded that the internal stress makes a small contribution to the work hardening and contributes to less than 10% of the total flow stress during monotonic loading at strains larger than 5%. The work hardening behavior has been correlated to the corresponding microstructure and the strengthening mechanisms are discussed.

Key words: aluminum alloys; mechanical characterization; strain hardening;

1. Introduction

Dispersion hardening caused by non-shearable particles is an important mechanism to strengthen materials. While precipitates are the essential strengthening phase in heat-treatable alloys, the dispersoids precipitated in non-heat-treatable aluminum alloys usually have a smaller contribution to the strength, due to their relatively low number density and large size. Still the dispersoids can have a considerable influence on the strengthening of the non-heat-treatable alloys. Recently it is reported that by optimizing the heat treatment, dispersoids of high density and small size can be achieved in 3xxx aluminum alloys, which can significantly increase the strength of the alloy [1].

Dispersoids also affect work hardening behavior of metals. Early research works have reported the work hardening behavior of dispersion-hardened copper crystals during tensile tests and the corresponding dislocation structure [2-5]. It was found that a small volume fraction of dispersoids in pure copper single crystals resulted in a parabolic work hardening at small strains, which was different from the linear work hardening in single crystals without dispersoids [2]. At larger tensile strains, the crystal showed a work hardening similar to the matrix material [2]. A similar effect of dispersoids on work hardening during tension tests is also found in aluminum alloys [6-7]. A cross-over effect in stress-strain curves of an AA3207 alloy with and without dispersoids was observed [8]. It showed that in stage III the work hardening rate of the alloy with dispersoids decreased more rapidly than the alloy without dispersoids [8]. A similar effect was also observed in an AA6111 alloy with varied Fe and Mn levels [7], but the particles were not characterized. Only a few studies have considered the work hardening behavior of aluminum alloys containing dispersoids at large strains [9-10]. Research on a cold rolled aluminum containing 4% nano-size alumina particles showed that the strength of the alloy reached a maximum at a strain of ~1, and decreased slightly with further increased strain [9-10].

TEM investigations [3, 5, 11] show that dislocation loops form around dispersoids as Orowan loops or prismatic loops during deformation, resulting in a high dislocation density. These dislocation loops are often referred to as geometrically necessary dislocations (GNDs), and can be converted to helices or dipoles [5]. A high density of dispersoids enhances the tendency for dislocations to arrange into a cell structure [9-10], leading to a reduced cell size compared to single-phase materials [3, 9, 12].

The effect of dispersoids on the yield strength is generally explained by the well-known Orowan bypass mechanism, as reviewed by several authors [13-15]. However, the influence of dispersoids on work hardening can not be explained by one single mechanism. In the literature it has been explained by either long-range internal stress or dislocation interactions. Fisher et al. [16] first proposed that the work hardening of dispersion-hardened metals was attributed to the long-range internal stress due to the

dislocation loops around dispersoids. Later Brown and Stobbs [17-18] established a theory of work hardening based on internal stress, using elastic continuum mechanics. Ashby [2, 19] proposed a model of work hardening based on the interactions between gliding dislocations and GNDs. Hirsh and Humphreys [4] proposed a similar model as Ashby's to explain the work hardening of dispersion-hardened single crystals of copper alloys. Recent research on aluminum alloys containing precipitates or dispersoids agrees that both internal stress and dislocation interactions contribute to the work hardening [20-21].

In previous experimental studies [8-10] alloys with dispersoids has been compared to alloys without dispersoids, but also probably with different levels of solutes. This difference in the solute content made it difficult to directly conclude on the influence of dispersoids on work hardening behavior. Furthermore, very few experimental results have been reported on dispersion hardened materials deformed more than what can be achieved by tensile tests. In order to reveal solely the dispersoid influence on work hardening behavior, the solute content needs to be well controlled. In the present work, a set of carefully designed heat treatments are carried out to generate the same solid solution levels but different number densities of dispersoids in a model Al-Mn alloy. The influence of dispersoids on strengthening and work hardening behavior at moderate and large strains is investigated.

2. Experimental

The material used in this study was an Al-Mn-Fe-Si direct chill cast billet with a diameter of 228 mm produced by Hydro Aluminum, following the standard casting practice with respect to grain refiner addition and casting speed. The chemical composition of the alloy (wt %) was: Mn 0.97, Fe 0.50, Si 0.15 and others 0.05. Samples for cold rolling and tensile tests were cut from the half radius location of the ingot. The average grain size and secondary dendrite arm spacing of the as-cast alloy were measured as 103.6 and 28.2 μm, respectively, by using a lineal intercept procedure with optical microscope. A homogenization heat treatment was conducted in an air circulation furnace. Four different homogenization procedures were designed to obtain two different solute levels and for each of the solute levels to obtain two different size

distributions of dispersoids. The detailed homogenization procedures are listed in Table 1. The labels “A” and “B” represent the solid solution levels of Mn in the alloy, while the labels “H” and “L” represent high and low number densities of dispersoids, respectively in the as-homogenized materials. The electrical conductivity of the as-homogenized materials was measured by using a Foerster Sigmatest 2.069 and applied to evaluate the solid solution level of Mn. The solid solution levels of different alloying elements of BH and BL were also estimated from the measurements of the thermoelectric power (TEP) at Hydro Aluminum Deutschland GmbH R&D center, Bonn.

Table 1 Homogenization treatments

	Homogenization before water quenching
AH	50 K/h from room temperature (RT) to 823K
AL	50 K/h from RT to 873K, held 8h
BH	50 K/h from RT to 723K, held 4h
BL	50 K/h from RT to 873K, held 4h + 25 K/h to 773K held 4h

After homogenization, BH and BL samples were rolled at room temperature in a laboratory mill down to about 1.5mm in thickness to achieve von Mises strains of 0.74, 1.8, and 3.3 (nominal reduction 50%, 80%, and 95% respectively). AH and AL were rolled with reductions of 30%, 50% and 80%.

The microstructure of the alloy after homogenization and tension testing to the strain of 0.16 was observed in a JEOL 2010 transmission electron microscope (TEM) at 200KV. The TEM foils were cut from the cross section plane of the deformed specimens. TEM foils were prepared by twin-jet electropolishing in an electrolyte containing two parts methanol and one part nitric acid at 253K and 20V. The as-homogenized microstructure and deformation structure after rolling were observed by backscattered electron channeling contrast (BSE-ECC) imaging at 15KV in a Zeiss Ultra 55 field emission gun scanning electron microscope (SEM).

Tensile testing of the homogenized materials was performed using cylindrical

specimens with a diameter of 6 mm. The specimens for tensile tests of the rolled materials were 6 mm wide and 1.5 mm thick. The extensometer gauge length was 25 mm. An MTS 810 hydraulic testing machine was applied for tensile tests under a constant ramp rate at room temperature, giving a strain rate of $\sim 10^{-3}\ s^{-1}$. The specimens for the Bauschinger tests were 7 mm in diameter and their parallel length was 20 mm. The extensometer gauge length was 10 mm. The tests were carried out first in tension and then in compression, or in the opposite order. The strain rate was $\sim 10^{-4} s^{-1}$. Most of the investigations were carried out on BH and BL. The samples AH and AL were used to complement the experimental results of BH and BL.

3. Results

3.1 As-homogenized microstructure

The measured values of the electrical conductivity of the as-homogenized materials are shown in Table 2. AH and AL have nearly the same electrical conductivity. That is also the case for BH and BL. It implies that AH has similar solute concentration to AL and also BH and BL have about the same solute level. A further quantitative evaluation on the Mn contents in solid solution can be performed based on the relationship between the electrical conductivity (*EC*) and the concentration of alloying elements in solid solution, which is adapted from Ref. [22]:

$$1/EC = 0.0267 + 0.032\ \text{Fe\%} + 0.033\ \text{Mn\%} + 0.0068\ \text{Si\%} + 0.0021\ \text{Particle\%}, \quad (1)$$

where Fe%, Mn%, Si% are the weight percentages of the amounts of these elements in solid solution, and Particle% is the total volume fraction of particles. Since the concentration of Si in solid solution was very small (the Si% values measured by TEP were in the range of 0.01~0.02wt% in BH and BL), it influences the electrical conductivity much less than Fe and Mn. Thus, the Si% was set to be constant, 0.01wt% in the calculation. The concentration of Fe in solid solution is very small due to its low solubility and is therefore negligible. Then the Mn content in solution could be calculated from the electrical conductivity. The results are listed in Table 2. As can be seen, two levels of solutes in solid solution, a high level of Mn in AH and AL compared to a low level in BH and BL were achieved.

Table 2 The electrical conductivity (*EC*), concentrations of solutes, the diameters and

fractions of particles.

	EC, MS/m	Mn, wt%	Constituent particles		Dispersoids		
			Diameter, μm	Area fraction	Diameter *d*, μm	Volume fraction f_V	Spacing L_d, μm
AH	21.3	0.39	1.4	3.1%	0.09	0.32%	1.08
AL	21.3	0.38	1.6	3.5%	0.12	0.16%	1.53
BH	24.0	0.25	1.0	2.4%	0.11	0.81%	0.85
BL	23.8	0.26	1.5	2.8%	0.16	0.41%	1.37

The morphology and distribution of the constituent particles in BH and BL are shown in Figure 1. The constituent particles in BL were coarser than those in BH, which is due to the coarsening of particles during long time homogenization at a higher temperature. A detailed study on the evolution of constituent particles in a similar alloy during homogenization can be found in Ref. [23]. The diameter and area fraction of constituent particles and dispersoids have been measured by a quantitative image analysis of SEM images and the results are shown in Table 2. It should be noted that the observed surface was not an ideal two-dimensional section, since the coarse particles are protruded out of the surface section. Thus, the measured area fraction of coarse constituent particles is larger than the volume fraction. α-Al(Mn,Fe)Si dispersoids can also be observed in the SEM images (Fig.1). Obviously, the number density of dispersoids in BH is much higher while their size is much smaller than in sample BL. Precipitate free zones (PFZs) around dendrite and grain boundaries were observed in AL and BL. The area fraction of PFZs, f_{PFZ} in BL was ~40%, determined by the manual point count procedure from SEM images (according to ASTM E562-08). The number density of dispersoids was measured by SEM, and the local volume fractions of dispersoids excluding PFZs, f_{LV} were calculated according to [22]. The volume fractions in BL and AL include the PFZs. The total volume fraction including PFZs, f_V is given by $f_{LV}(1-f_{PFZ})$, as shown in Table 2. The dispersoid spacing excluding PFZs, L_d, from center to center, was calculated as [6]:

$$L_d = d\sqrt{\frac{\pi}{6 f_{LV}}}. \qquad (2)$$

The dispersoid size distribution fits a lognormal distribution, as shown in Fig. 1d.

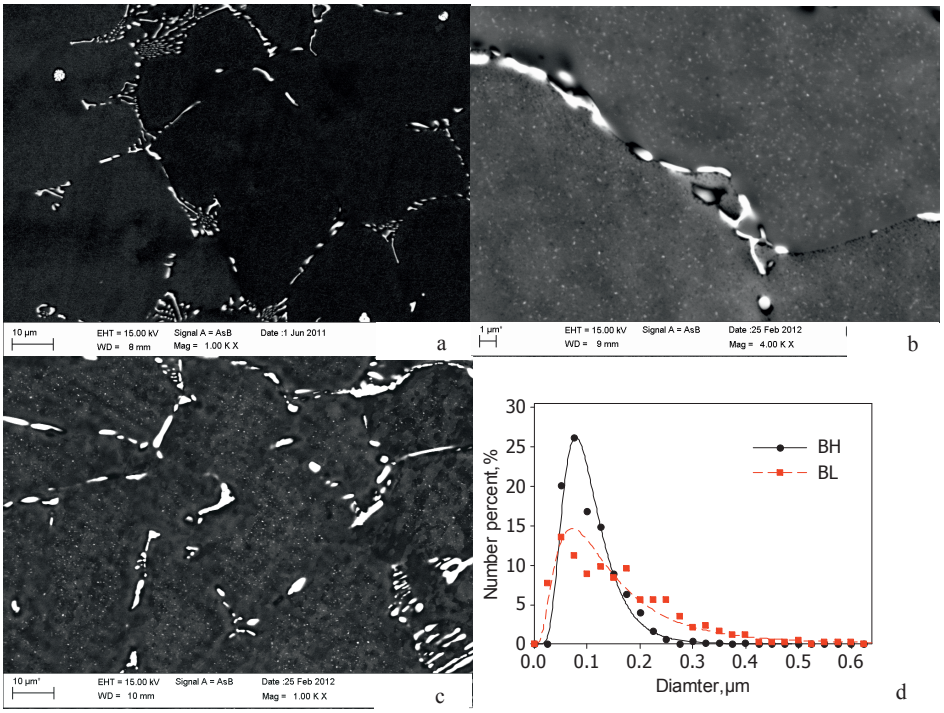

Fig.1 Back-scattered electron images of BH and BL and their size distribution of dispersoids. (a) shows the distributions of the constituent particles in BH; (b) shows the distribution of dispersoids in BH at a higher magnification; (c) shows the non-uniform distributions of constituent particles and dispersoids in BL; d) the size distribution of dispersoids in BH and BL with lognormal fitting curves.

3.2 Microstructure after tensile deformation

Figure 2 shows examples of dislocation structures of BH and BL at a tensile strain of 16%. The influence of dispersoids on the dislocation structure evolution can be clearly seen by comparing BH (Fig. 2a) and BL (Fig. 2b). In BH a large amount of relatively loose dislocation tangles have formed around the dispersoids, forming dislocation networks. Most of the dislocations are connected to cell walls. In comparison to BH, the dislocation density is lower while the cell size is larger in BL.

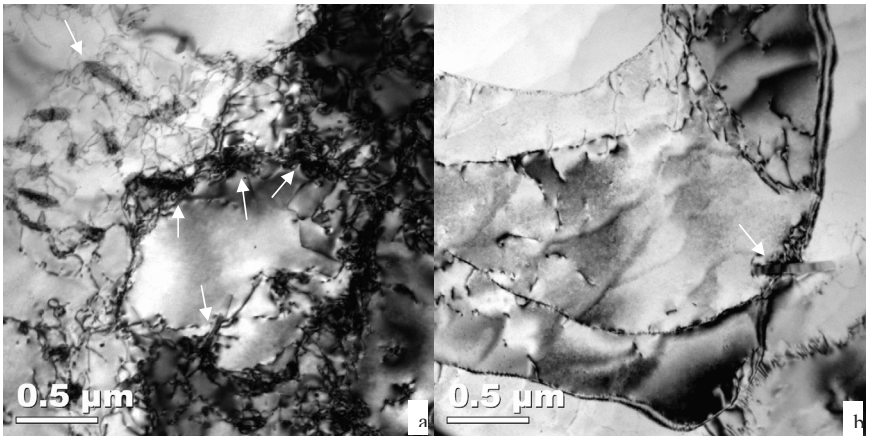

Fig. 2 TEM bright field images of the cross sections of BH (a) and BL (b) at 16% tension strain. Cell walls formed by connecting dislocation networks around dispersoids (indicated by the arrows).

The average cell size was measured from TEM images. Two orthogonal diameters, d_1 and d_2, were measured for each cell. The cell size is calculated as the square root of $d_1 \times d_2$. An average cell size was obtained by 50-70 measurements of cells. The cell sizes of BH and BL at 16% tensile strain are listed in Table 3. The cell sizes of AH and AL were 0.92 µm and 1.03 µm respectively, which are close to their interspacing of dispersoids (Table 2). The cell size of the sample containing a high-density of dispersoids was smaller than those containing a low-density of dispersoids, and the difference in cell size was statistically significant according to the Student's one-tailed t-test (significance level =0.01 for BH and BL).

3.3 Microstructure after cold rolling

The subgrain structure formed during cold rolling is shown in Figure 3. The subgrains are elongated along the rolling direction. The average subgrain sizes parallel and perpendicular to the elongation direction of the subgrains were measured by lineal intercept procedures from SEM images. The number of subgrains intercepted by one straight line is about 10~40, and two or three measurements were done in each area to give an average value of both d_x and d_y. The square root of $d_x \times d_y$ is taken as the 2D subgrain size. Thus, the subgrain size measured by SEM may not be quantitatively

comparable to the cell size measured by TEM. The standard deviation was based on three or four areas measured for each sample, and indicates the uniformity of the subgrain structure between different grains, not the individual measurement deviation.

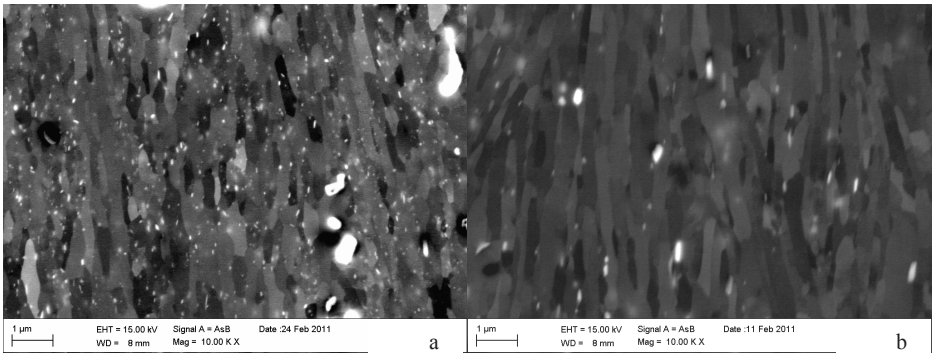

Fig.3 SEM backscattered electron images of subgrain structure and dispersoids of sample BH (a) and BL (b) at a strain of 3.3. The images were taken in the ND-RD section (the vertical direction is RD).

As can be seen in Table 3, the subgrain size deviation of BL at a strain of 0.74 was relatively large, indicating a non-uniform subgrain structure. BL contains ~40% PFZs, in which the evolution of the subgrain structure at small strains may be different from those containing dispersoids. At larger strains, the subgrain structure appears uniform, as shown in Fig.3, consistent with the small standard deviations in Table 3. Deformation zones around constituent particles contained smaller subgrains, which were observed, but not counted and considered in this work. The subgrain structures of both BH and BL were similar at large strains. The subgrain size decreases with increasing rolling strain, and the mean subgrain sizes of BH and BL are similar when the deformation strain exceeds 0.74, indicating that dispersoids do not have a significant influence on the subgrain size at large strains.

Table.3 The cell/subgrain sizes (µm) during tension or rolling.

von Mises strain	0.16	0.74	1.8	3.3
BH	0.85±0.28	1.10±0.01	0.49±0.04	0.42±0.01
BL	1.01±0.29	0.96±0.39	0.50±0.05	0.46±0.04

*The cell/subgrain size and standard deviation are defined in the text. The differences in the methods and definitions have also been noted in the text.

At large strains the dispersoids were observed mainly at subgrain boundaries. The number fraction of dispersoids located at the subgrain boundaries was estimated from the BSE-ECC images (e.g. Fig.3). The number fractions of dispersoids at subgrain boundaries at strains of 1.8 and 3.3 were ~80% in BH, and ~90% in BL. At large strains most of the dispersoids are located at subgrain boundaries in both materials. The number fraction is roughly estimated, because some of the subgrain boundaries with small misorientations can not be identified in BSE-ECC images due to the limited resolution and the unfavorable orientations of some subgrains. Dispersoids reflect more back-scattered electrons and have higher contrast than the aluminum matrix, so the observed dispersoids can be deep beneath the surface while only the trace of the subgrain boundary can be observed at the surface. It is also possible that a dispersoid was incorrectly observed at a subgrain boundary because of projection. Thus, the number fraction is just roughly estimated.

3.4 Strength and work hardening

The stress-strain curves from tensile tests of as-homogenized materials are shown in Fig.4. At the initial deformation stage (strain <0.02), a smaller dispersoid spacing led to a higher flow stress as well as a higher work hardening rate. The yield strength of BH is much larger than that of BL. The 0.02% offset yield strength of BH and BL was 37 MPa and 24 MPa, respectively. The 0.2% offset yield strength of BH and BL was 56 MPa and 37 MPa, respectively. The work hardening of BH in the range from 0.02% to 0.2% plastic strain contributes to a strength increase ~19 MPa, much larger than that of BL (~13MPa). This indicates a higher work hardening rate due to a high density of dispersoids.

The ultimate tensile strength (UTS) of as-rolled materials is plotted as a function of the von Mises strain in Fig.4. The trend lines connecting stress-strain curves of as-homogenized materials and the UTS of rolled materials indicate the work hardening behavior at large strains. The flow stresses of BH and BL approach each other with increasing strain, and finally converge at large strains, although the initial yield stresses are quite different. The Taylor factors were calculated from textures measured by X-ray

diffraction. The Taylor factors of BH and BL are similar at the same strain. The Taylor factors of both samples under uniaxial tension along RD do not change at strains less than 0.74 and they increase slowly from 3.1 to 3.2 at larger strains for both BH and BL. The convergence of the stress-strain curves of BH and BL (Fig.4) indicates that the influence of dispersoids on flow stress diminished at large strains. The Vickers hardness (HV) of AH and AL is also plotted in Fig. 4. The hardness curves of AH and AL have converged at strain of 0.4. The standard deviation of HV measurements is less than 3% of HV.

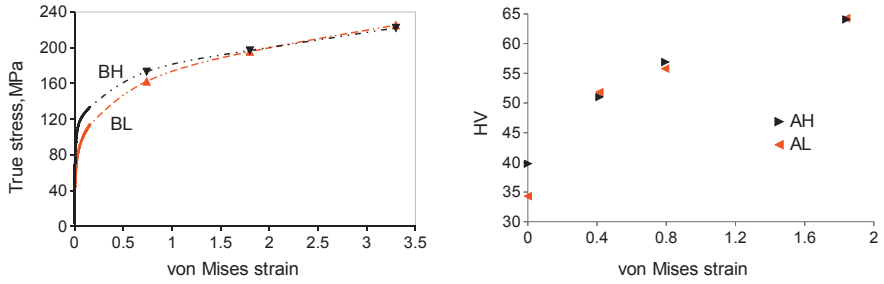

Fig.4 (a)Stress-strain curves of as-homogenized BH and BL (solid lines) and the ultimate tensile strength of materials rolled to various logarithmic strains (▼: BH, ▲: BL) (dashed lines are trend lines);(b) Vickers hardness (HV) of AH and AL in as-homogenized and rolled conditions.

3.5 Bauschinger effect

Pile-up of Orowan loops around non-shearable particles leads to an elastic internal stress, which is often referred as kinematic hardening. Internal stress due to particles may play an important role in plastic deformation of dispersion hardened materials, and can be observed during reversed strain paths, e.g. Bauschinger tests. The Bauschinger effect is illustrated in Fig.5, where it is compared to monotonic loading. The specimen was first deformed in tension to a prescribed forward plastic strain, and then the deformation was reversed in compression. The specimen started to buckle at 1-2% compression strain. The opposite case with prestrain of ~1% in compression and then tension tested is also shown in Fig.5. For this case the reverse stress approaches the monotonic curve, converging at a strain of ~0.1, suggesting that the reduced strength after the reversal is not permanent.

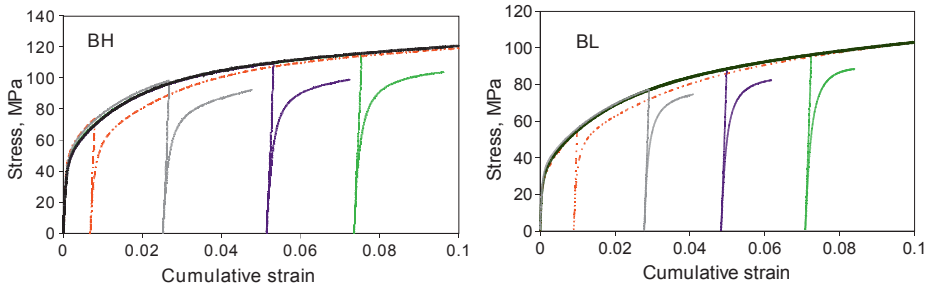

Fig.5 Forward-reverse stress -cumulative strain curves following different forward plastic strains. Solid lines: tension-compression; dashed lines: compression-tension tests.

As previously suggested in [20, 24-25], the Bauschinger stress equals half of the difference between the monotonic and the reversed stress-strain curves. The Bauschinger stress obtained from Fig.5 is shown in Fig.6, and is comprised of two parts: Firstly a rapid reduction at small reverse strains (<0.004); secondly a regime where the Bauschinger stress decreases slowly in a nearly linear manner with increasing strain. The first transient part involves inhomogeneous local stresses and complex dislocation rearrangements [25-26], which is not further considered in present work. The subsequent regime indicates an almost steady-state Bauschinger stress. The Bauschinger stress at the reverse strain of 1% is used as the ‘‘steady-state” internal stress σ_b. The results are shown in Fig.7. The internal stress σ_b increases with increasing plastic strain, and it starts to saturate at a strain of ~5%.

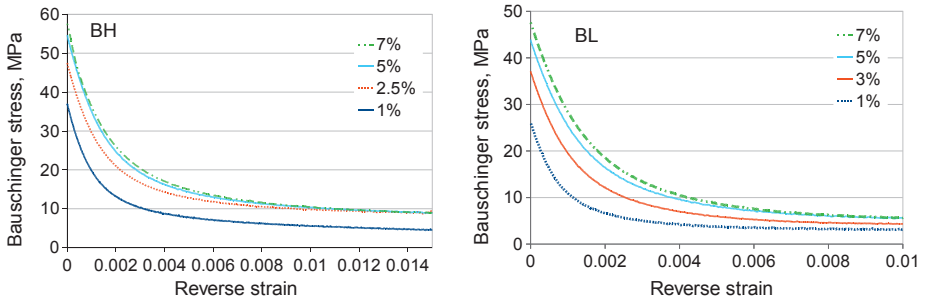

Fig.6 Bauschinger stress as a function of reverse strain.

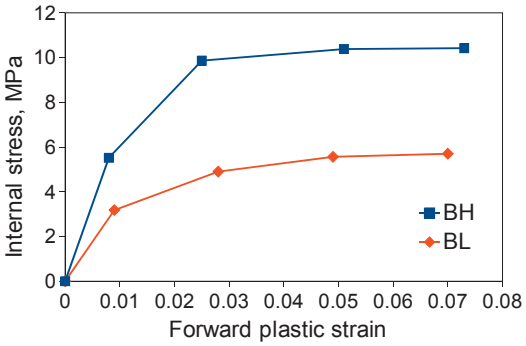

Fig.7 Evolution of internal stress as a function of the forward plastic strain.

4. Discussion

4.1 Influence of dispersoids on the evolution of the cell structure

A cell structure forms during deformation as the result of trapping and annihilation of dislocations. Dislocation loops (GNDs) form around dispersoids during deformation, in the form of Orowan loops around dispersoids, rows of prismatic loops in the vicinity of dispersoids, and dislocation helices or dipoles as well [5, 11]. The extra GNDs formed due to dispersoids result in a high local density of dislocations, providing more trapping sites for gliding dislocations. Dislocation networks or tangles tend to form at these preferable sites. The prismatic loops emitted from adjacent dispersoids may interact by trapping and annihilating each other. The particles act as sources of GNDs that contribute to the building of new cell walls. New cell walls can form by connecting the fragments of dislocation tangles, as indicated by TEM observations in Fig. 2. The dispersoids and GNDs promote cell wall formation, leading to reduced cell sizes at small strains, which is observed in this work (Table 3) and also reported before [9, 12]. It is concluded that the magnitude of the reduction of cell size is related to the dispersoid spacing (or density), i.e. the smaller dispersoid spacing, the smaller cell size. However, if the dispersoid spacing is very small, the density of GNDs may be so high that this dislocation distribution dominates and appears uniform in the matrix. Then the formation of cell walls would be suppressed and the formation of subgrains is retarded, as observed in an Al-Sc alloy with a dispersoid spacing of 100 nm [27].

The effect of dispersoids on cell formation also changes with the deformation strain. As the strain increases, the cell size becomes smaller. When the cell size is reduced to a smaller size than dispersoids spacing, the effect of dispersoids on cell formation diminishes. As can be seen in Table 3, the subgrain sizes of BH and BL are both found to be similar, ~0.5 μm at strains larger than 1.8. This is smaller than the dispersoid spacing (0.9-1.4 μm in Table 2). Hansen and Bay [28] also found that neither the content nor the distribution of fine dispersed particles (0.6-1.2 wt% Al_2O_3) affected the subgrain size significantly after 50-90% drawing. The evolution of subgrains at large strains seems to be independent of the dispersoid spacing when the subgrain size becomes smaller than dispersoid spacing.

4.2 Yield strength

The coarse constituent particles distributed on dendrite and grain boundaries in the as-cast materials are of a low number density and large in size, so their contribution to dispersion hardening by the Orowan bypass mechanism is negligible. The Orowan stress is mainly due to the fine dispersoids. Thus, the yield strength is given by:

$$\sigma_y = \sigma_0 + \sigma_{SS} + \sigma_{HP} + \sigma_{Oro}. \quad (3)$$

σ_0 is the friction stress of pure aluminum. σ_{SS} is solid solution hardening, for which an empirical relation for Al-Mn can be found in [29]. σ_{HP} is the Hall-Petch relation of the grain size effect given by [30]. Both σ_{SS} and σ_{HP} do not affect the comparison between BH and BL, since their solute contents and grain sizes are similar. σ_{Oro} is the Orowan stress due to fine dispersoids, which is given by

$$\sigma_{Oro} = 0.81\frac{MAGb}{2\pi\lambda}\ln\left(\frac{\pi d}{4b}\right). \quad (4)$$

The equation is given by [13]. M is the Taylor factor (M≈3 here); G is the shear modulus of aluminum (G=27 MPa); b is the Burgers vector (b=0.286 nm). $\lambda = 0.4d\left(\sqrt{\pi / f_V} - 2\right)$ is the dispersoid spacing (surface to surface) on a slip plane [6]. f_V and d are the volume fraction and diameter of dispersoids, respectively. The difference in yield stress between BH and BL is contributed by the Orowan stress, and then the value of the constant A is estimated by fitting the calculations to the experimental results. A becomes 1.2 by fitting to the 0.02% yield strength, and 1.8 by

fitting to the 0.2% yield strength. The value of A can also be estimated by $A = 1/\sqrt{1-\nu}$ given in [13] (where ν=0.34 is Poisson's ratio), and then equals 1.2. The dispersion-hardened material has a significantly higher initial work hardening rate than the matrix material. Thus, the fitted value of A increases with increased offset strain. To reduce the influence of the initial work hardening, the offset of the yield strength should be chosen as small as possible.

4.3 Bauschinger effect

The internal stress due to particles can be estimated based on Eshelby's solution [20] as

$$\sigma_b = f_p E_p \varepsilon^* \quad (5)$$

E_p is the Young's modulus of particles, and f_p is the volume fraction of particles. ε* is the unrelaxed plastic strain and $\varepsilon^* \propto n/r$, where n is the number of Orowan loops hugging the particles and r is their radius [19]. This implies that the smaller size of the dispersoids in BH will lead to a larger internal stress than in BL. There is a large volume fraction of constituent particles in the alloy, which is much larger than the fraction of dispersoids (Table 2). These coarse constituent particles might produce tangles of secondary dislocations instead of Orowan loops, inducing an additional internal stress [18, 31].

There are two types of particles in the alloy regardless of being constituent particles or dispersoids: Al_6(Mn,Fe) and α-Al(Mn,Fe)Si. It is reported that the chemical composition of particles changes during homogenization and that the fraction of α-Al(Mn,Fe)Si particles increases [23]. This probably results in a difference between the Young's modulus for the particles in BH and BL. The shape of coarse constituent particles is not spherical or plate-like, and their shapes change during the homogenization. Therefore a quantitative comparison of internal stress according to Eq. (5) is difficult. A qualitative assessment of the contribution of the internal stress is attempted in the present work. The ratio of the internal stress to the monotonic flow stress at the same total strain is in the range of 5% to 10% in BH and BL at a forward plastic strain of 1-5%. The contribution from the internal stress to the total work hardening is estimated as $\sigma_b/(\sigma_F - \sigma_y)$, following the method used in [20]. Here σ_F is

the forward flow stress at the point of reversal, and σ_y is the 0.02% yield stress of the undeformed material. The ratio is shown as a function of the forward plastic strains in Fig.8. It increases rapidly at small strains ($\leqslant$1%), and from there it contributes ~16% and 10% in BH and BL respectively. The internal stress due to particles plays a minor role in work hardening after the initial stage, and this stress contribution is small compared to the overaged alloys in [20].

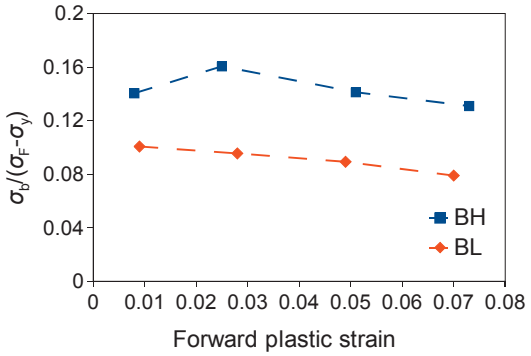

Fig. 8 The ratio of the internal stress to the increase in stress by work hardening as a function of the forward plastic strain.

4.4 Strengthening at small strains

The flow stress at small strains is assumed to be:

$$\sigma = \sigma_0 + \sigma_{SS} + \sigma_{HP} + \sigma_{Oro} + \sigma_i + \sigma_b = \sigma_y + \sigma_i + \sigma_b \,. \quad (6)$$

It is noted that a non-linear superposition of the hardening components has been discussed before [32-34]. The linear assumption is used for the sake of simplicity in the present work. The isotropic stress σ_i corresponds to the contribution from dislocation interactions: $\sigma_i = M\alpha Gb\sqrt{\rho}$, where α is a constant. The total dislocation density, ρ, includes statistically stored dislocations (i.e. forest dislocations), ρ_S, and GNDs, ρ_G, i.e. $\rho = \rho_S + \rho_G$. Many models have been proposed for the evolution of forest dislocations but this is not the topic in this work. The evolution of GNDs is often modeled following Ashby's approach [19]. The magnitude of the isotropic hardening can be estimated from $\sigma_F - \sigma_y - \sigma_b$ as shown in Fig. 9. The difference between BH and BL in Fig. 9 is caused by different GND densities due to the different densities of

dispersoids. The maximum difference between σ_i for BH and BL is ~7MPa. This indicates that the magnitude of the contribution of GNDs to σ_i is similar as from σ_b in Fig. 7. In Fig. 9 the isotropic stress of BL approaches that of BH at strains larger than 0.08. This is probably caused by a stronger dynamic recovery in BH. A high density of dispersoids induces additional dislocations, but also accelerates dynamic recovery, as suggested in [34].

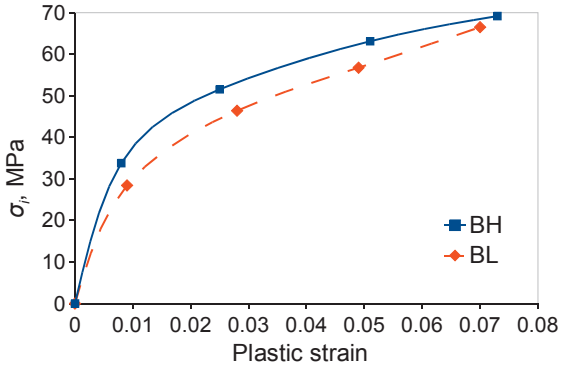

Fig.9 The calculated isotropic stress ($\sigma_i = \sigma_F - \sigma_y - \sigma_b$) as a function of the plastic strain.

In principle the internal stress is a long-range elastic stress from dislocation pile-ups at boundaries or particles. The contribution from the boundaries has been included in the Hall-Petch relation. The internal stress due to particles is found to saturate at a certain tensile strain, as shown in Fig.7 and by Ref. [20-21]. Thus, the internal stress does not contribute to the work hardening rate after its saturation. Moreover, the formation of deformation zones around coarse particles relieves the internal stress from the coarse particles. Thus, the internal stress becomes minor in the total flow stress at moderate and large strains. Work hardening at large strains is mainly attributed to the dislocation interactions.

4.4 Strengthening at large strains

At large strains, e.g. during rolling, the dislocation density inside subgrains has saturated, and the flow stress scales inversely with the subgrain size [35]. As discussed in section 4.1, the subgrain size is found not to be affected by dispersoids at large strains

(Table 3), where all the stress components except the Orowan stress are little affected by the dispersoids. The equal flow stresses of BH and BL suggest that the Orowan stress is absent at large strains. The Orowan stress is based on the bow out of gliding dislocations between dispersoids. Most of the dispersoids are tangled in subgrain boundaries or triple junctions, as shown in section 3.3. These barriers coincide with subgrain boundaries which are also barriers, but barriers at the same location should only be counted once. Hence, the Orowan stress can be neglected at large strains, where the flow stress of alloys containing dispersoids will approach that of the single-phase alloys. The strain at which the stress-strain curves converge depends on the dispersoid density (or spacing). A high dispersoid density (small spacing) is expected to lead to a convergence upon large strains. Note in Fig. 4 that AH and AL have the same Vickers hardness at a strain of 0.4, whereas the ultimate tensile strengths of BH and BL with a higher density of dispersoids have not converged until at a strain of 1.8. The flow stress after the convergence is affected by the solute content, but not by the dispersoids. The dispersion hardening is not effective at large strains.

5. Summary

A high density of fine dispersoids has been shown to strengthen the materials significantly, but their strengthening effect diminishes as the strain increases. The internal stress due to particles makes a contribution to the total work hardening (i.e. 10-20%) and starts to saturate at a tensile strain of 3-5%, although it increases rapidly at the initial stage of the deformation. The dislocation interactions, i.e. forest hardening, play the major role in the subsequent work hardening. Geometrically necessary dislocations, which are formed around dispersoids, enhance the formation of cell structure and lead to a reduced cell size. The dispersoids tend to be trapped in cell walls or subgrain boundaries. When the cell/subgrain size becomes smaller than the dispersoid spacing, the dispersoids do not affect the subgrain size and do not contribute to the strength any more. The flow stress is dominated by the dislocation substructure at moderate and large strains.

Acknowledgement

The authors are grateful for the assistance of Ning Wang and Pål Christian Skaret with SEM observations and tensile tests respectively. This work was funded by the Research Council of Norway, Hydro and Sapa Technology under the project MOREAL.

References

[1] Y.J. Li, A.M.F. Muggerud, A. Olsen, T. Furu, Acta Mater., 60 (2012) 1004-1014.
[2] M.F. Ashby, Philos Mag, 14 (1966) 1157-1178.
[3] M.H. Lewis, J.W. Martin, Acta Metall., 11 (1963) 1207-1214.
[4] P. Hirsch, F. Humphreys, Proc. R. Soc. London, A, 318 (1970) 45-72.
[5] F. Humphreys, P. Hirsch, Proc. R. Soc. London, A, 318 (1970) 73-92.
[6] N. Hansen, Acta Metall., 18 (1970) 137-145.
[7] J.D. Embury, W.J. Poole, D.J. Lloyd, Mater. Sci. Forum, 519-521 (2006) 71-78.
[8] B. Forbord, K. Marthinsen, E. Nes, Mater. Sci. Forum, 331-337 (2000) 557-564.
[9] C.Y. Barlow, N. Hansen, Acta Metall., 37 (1989) 1313-1320.
[10] C.Y. Barlow, N. Hansen, Y.L. Liu, Acta Mater., 50 (2002) 171-182.
[11] F.J. Humphreys, A.T. Stewart, Surf. Sci., 31 (1972) 389-421.
[12] D.J. Lloyd, D. Kenny, Acta Metall., 28 (1980) 639-649.
[13] L.M. Brown, R.K. Ham, Dislocation-particle interactions, in: A. Kelly, R.B. Nicholson (Eds.) Strengthening Methods in Crystals, Elsevier, Amsterdam, 1971, pp. 9-135.
[14] B. Reppich, Particle Strengthening, in: R.W. Cahn, P. Haasen, E.J. Kramer (Eds.) Materials science and technology: a comprehensive treatment, Wiley-VCH, Weinheim, 2005, pp. 311.
[15] V. Gerold, Precipitation hardening, in: F.R.N. Nabarro (Ed.) Dislocations in solids, North-Holland, New York, 1979, pp. 219-260.
[16] J.C. Fisher, E.W. Hart, R.H. Pry, Acta Metall., 1 (1953) 336-339.
[17] L.M. Brown, W.M. Stobbs, Philos Mag, 23 (1971) 1185-1199.
[18] L.M. Brown, W.M. Stobbs, Philos Mag, 23 (1971) 1201-1233.
[19] M.F. Ashby, Philos Mag, 21 (1970) 399-424.
[20] H. Proudhon, W.J. Poole, X. Wang, Y. Bréchet, Philos Mag, 88 (2008) 621-640.
[21] G. Fribourg, Y. Bréchet, A. Deschamps, A. Simar, Acta Mater., 59 (2011) 3621-3635.
[22] Y.J. Li, L. Arnberg, Acta Mater., 51 (2003) 3415-3428.
[23] Y.J. Li, L. Arnberg, Mater. Sci. Eng., A, 347 (2003) 130-135.
[24] D.V. Wilson, Acta Metall., 13 (1965) 807-814.
[25] J.D. Atkinson, L.M. Brown, W.M. Stobbs, Philos Mag, 30 (1974) 1247-1280.
[26] W.Z. Han, A. Vinogradov, C.R. Hutchinson, Acta Mater., 59 (2011) 3720-3736.
[27] P.J. Apps, M. Berta, P.B. Prangnell, Acta Mater., 53 (2005) 499-511.
[28] N. Hansen, B. Bay, J. Mater. Sci., 7 (1972) 1351-1362.
[29] Ø. Ryen, O. Nijs, E. Sjölander, B. Holmedal, H.E. Ekström, E. Nes, Metall. Mater. Trans. A, 37 (2006) 1999-2006.
[30] N. Hansen, Acta Metall., 25 (1977) 863-869.
[31] L.M. Brown, W.M. Stobbs, Philos Mag, 34 (1976) 351-372.
[32] U.F. Kocks, A.S. Argon, M.F. Ashby, Prog. Mater. Sci., 19 (1975) 1-281.
[33] Y. Dong, T. Nogaret, W.A. Curtin, Metall. Mater. Trans. A, 41 (2010) 1954-1960.

[34] J. da Costa Teixeira, L. Bourgeois, C.W. Sinclair, C.R. Hutchinson, Acta Mater., 57 (2009) 6075-6089.
[35] E. Nes, Prog. Mater. Sci., 41 (1997) 129-193.

Article 2

Modeling work hardening of aluminum alloys containing dispersoids

Qinglong Zhao, Bjørn Holmedal
Department of Materials Science and Engineering, Norwegian University of Science and Technology, Trondheim N-7491, Norway

Abstract: The influence of dispersoids on tensile deformation behavior has been studied by comparison of aluminum alloys containing different dispersoid densities. It was found that a fine dispersion of non-shearable particles led to an increased work hardening at the initial plastic deformation, but the effect was opposite at higher strains. The reason has been attributed to the generation of geometrically necessary dislocations (GNDs). A new model has been proposed for the evolution of GNDs based on a balance of storage and dynamic recovery of GNDs. The model predicts a rapid saturation of GNDs and a reduced work hardening at small strains, consistent with the experimental results.

Keywords: strain hardening; dispersion strengthening; aluminum alloys; modeling; microstructure

1. Introduction

The work hardening of metals has been studied for decades, and is still a topic of interest, especially in solid solution or two-phase materials containing particles. Early research [1] reported that a small volume fraction of dispersoids in pure copper single crystals resulted in a parabolic hardening, as compared to a more linear initial hardening in single crystals without dispersoids. At higher strains the crystal shows a work hardening similar to the matrix material. Similar dispersoid effect on the work hardening is also found in commercial alloys [2]. The initial parabolic hardening is related to a rapid increase in the dislocation density due to the presence of dispersoids [3-4], where dislocation loops form around the dispersoids [5]. The extra dislocations formed due to non-shearable particles are geometrically necessary dislocations (GNDs). Humphreys and Stewart [6] observed by TEM and described the configurations of GND loops in brass containing dispersoids. The GNDs are difficult to observe precisely, since they tend to anneal out by the electron beam. Theories for the work hardening based on the generation of GNDs in the form of shear loops or prismatic loops were proposed by Ashby [7-8] and summarized in [9] to explain the initial work hardening in tensile tests.

Ashby provided an estimate for the largest strain, for which the prismatic loops remain stable. This might be interpreted as a cut off strain for the athermal storage of GNDs, but this was not explicitly included as a mathematical model. Brown and Stobbs [10-11] proposed a framework based on internal stress to describe work hardening including the Bauschinger effect. Recently Proudhon et al.[12] proposed a model of internal stress following the approach of Brown and Stobbs [10] to calculate the unrelaxed plastic strain, and assume that the number of Orowan loops around particles saturates at certain strains. This assumption is also used in other recent models, as in [13-14] using the maximum number of Orowan loops around a particle as an input parameter that is fitted to the experimental curves of the specified alloy.

Only a few works [2, 15-16] consider the remaining part of the stress-strain curve subsequent to the initial steep hardening of aluminum alloys with dispersoids. The current authors investigated the influence of dispersoids on work hardening during tension and rolling [article 1]. It was found that the work hardening rate of the alloy with dispersoids decreased more rapidly than the alloy without dispersoids after the initial deformation. This is related to the storage and dynamic recovery of the GNDs during deformation at room temperature. The recovery of GNDs was first ascribed to the climb and annihilation of Orowan loops by pipe-diffusion [4, 17]. The detailed modeling of work hardening incorporating this recovery mechanism produced a too strong temperature dependency of work hardening compared to the experimental results [18]. In a recent model [16] it is assumed that the GND density increases athermally at small strains and saturates immediately at a specific critical strain. The GND saturation density was determined by a scaling relation with a reference alloy. Their modeling fitted the experiments well, but does not account for that the solute content of the modeled alloy could be different from the reference alloy and therefore affect the dynamic recovery differently.

The aim of the present paper is to establish a simple dislocation based model of monotonic work hardening incorporating a quantitative analysis of dispersoids. A set of Al-Mn alloys with controlled solute contents was used in this work, modeling the influence of dispersoids on work hardening. A new model for the recovery of GNDs is

proposed and discussed, where the basic idea is a scaling between the saturation density of dislocations in the matrix and the local saturation density of GNDs.

2. Experimental

The material was an Al-Mn-Fe-Si direct chill cast billet. The details of heat treatments have been described in [article 1]. The treatments were designed to give two different dispersoid distributions, a low density labeled "BL" and a high density labeled "BH". The coarse constituent particles, α-Al(Mn,Fe)Si and Al_6(Mn,Fe), formed at dendrite and grain boundaries during casting. The particles became coarser and spheroidized during homogenization at a high temperature. Dispersoids, α-Al(Mn,Fe)Si and Al_6(Mn,Fe) precipitated during the homogenization. The diameters and fractions of dispersoids and constituent particles are listed in Table 1. Precipitate free zones (PFZs) around constituent particles were observed in BL. The area fraction of PFZs was estimated to be ~40% from the backscattered electron images [article 1]. The details of microstructure can be referred to [article 1].

Table 1 The concentrations of solutes, the diameters and fractions of particles.

	Mn, wt%	Constituent particles		Dispersoids	
		Diameter, μm	Area fraction	Diameter, μm	Volume fraction
BH	0.25	1.0	2.4%	0.11	0.81%
BL	0.25	1.5	2.8%	0.16	0.41%

In Fig. 1 the influence of dispersoids on the work hardening is shown by the Kocks-Mecking plot. The offset of the yield stress is set as 0.2%. The work hardening rate of BH containing the high dispersoid density was higher at first, but decreased more at a later stage. The work hardening rate of BH is lower than that of BL at σ-σ_y larger than 45 MPa (Fig. 1).

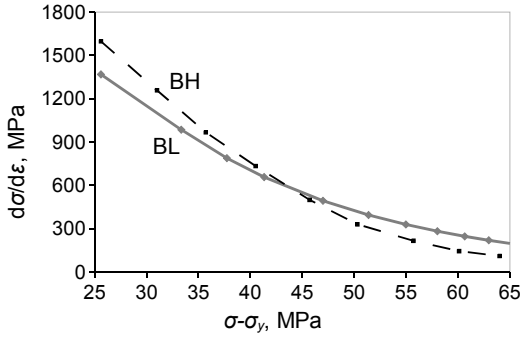

Fig.1 Kocks-Mecking plots of BH (dashed line) and BL (solid line), showing that the work hardening rate of BH is initially higher than BL but lower at higher strains.

3. Modeling of work hardening at small strains

The work hardening at small strains of materials containing particles is composed of isotropic hardening due to dislocation interactions and kinematic hardening caused by elastic inclusions, such as particles, as discussed in [article 1]. A linear superposition of the hardening components is used for the sake of simplicity. The flow stress σ is described as

$$\sigma = \sigma_y + \sigma_i + \sigma_b . \quad (1)$$

The strengthening mechanism for the yield stress σ_y has been discussed in [article 1]. σ_i is the isotropic hardening, and σ_b is the kinematic hardening. σ_b can be measured as the internal stress from Bauschinger tests. Proudhon et al. [12] proposed a model of kinematic hardening where the storage of Orowan loops at particles saturates at certain strains. This model has been applied in [13-14]. It produces a Voce type saturation of the internal stress, and hence is formulated as

$$\sigma_b = \sigma_{b,s}\left[1-\exp\left(-\frac{k_b\varepsilon}{\sigma_{b,s}}\right)\right]. \quad (2)$$

$\sigma_{b,s}$ is the saturated internal stress, and k_b is a constant. Eq. (2) is applied to fit the experimental results. The results are shown in Fig. 2, where the experimental results are well fitted.

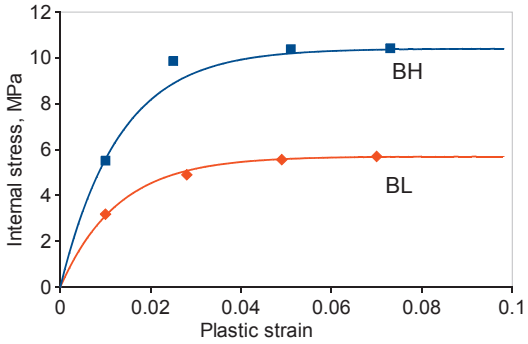

Fig.2 The evolution of the internal stress as a function of the plastic strains with fitting curves of Eq. (2) (symbols: experimental measurements from [article 1]).

A model of isotropic hardening is established to quantitatively explain the work hardening behavior at small strains. The stress contribution of the dislocation interactions to work hardening is given by

$$\sigma_f = M\tau_f = M\alpha Gb\sqrt{\rho}\,, \tag{3}$$

where α is a constant about 0.3, G=26 GPa is the shear modulus of aluminum and b is Burgers vector (0.286 nm). The Taylor factor M changes very little in tension tests due to the small deformations involved, hence it is taken as a constant equal to 3 for the random as-cast texture. To keep the theory as simple as possible, the modeling of the evolution of the statistically stored dislocation density in single-phase matrix, ρ, follows the one-parameter Kocks-Mecking approach [19]:

$$\frac{\mathrm{d}\rho}{\mathrm{d}\gamma} = k\sqrt{\rho}\left(1-\sqrt{\frac{\rho}{\rho_s}}\right). \tag{4}$$

Here γ is shear strain, γ=εM, where ε is the plastic strain. k is a storage constant which can be evaluated as $2\theta_{\mathrm{II}}/(\alpha bG)$, where θ_{II} is the work hardening rate of initial stage II [19-20]. In this simple one-parameter approach the dislocation density saturates towards ρ_s, which is the only parameter related to the dynamic recovery. Still a good description can be obtained for small strains relevant for the first part of the stress-strain curve of a tensile test. The statistical dislocation saturation density, ρ_s depends on the strain rate, temperature and the solute content. It has to be evaluated by fitting to the experimental results. For a prescribed constant strain rate and temperature, i.e. keeping ρ_s constant, the analytical solution of Eq. (4) is:

$$\sqrt{\rho} = \sqrt{\rho_s} + \left(\sqrt{\rho_0} - \sqrt{\rho_s}\right)\exp\left(-\frac{k\gamma}{2\sqrt{\rho_s}}\right). \quad (5)$$

Here ρ_0 is the initial dislocation density. The combination of Eq. (3) and Eq. (5) results in the Voce work hardening curve. The nominal strain rate and temperature remain constant here, and the solute contents of BH and BL are similar, so the parameters in Eq. (5) are the same for BH and BL.

The presence of non-shearable dispersoids leads to the formation of GNDs, which can be in the form of shear loops or prismatic loops. The shear loops around particles contribute as part of the internal stress σ_b. The volume fraction of dispersoids is much less than the coarse constituent particles, so their contribution to internal stress should be weaker than the coarse particles. The evolution of the internal stress is covered by Eq. (2). Prismatic loops can form in the vicinity of dispersoids by cross slip of shear loops as described in [5, 11]. In Ashby's theory [7-8], the prismatic loops should be both interstitial and vacancy types, and without annihilations the number of each type around each dispersoid of radius r becomes $n=2r\gamma/b$. However, TEM observations [5-6] show that most of the prismatic loops are interstitial type, implying that the loops of vacancy type are less stable. According to Ashby's theory [7] the total length of the GND loops formed around each dispersoid, counting both interstitial and vacancy type, equals $24\eta r^2\gamma/b$, where η is a factor which takes the shape of particles and the type of loops into account. The value of η will be reduced if the shape of dispersoids is changed from cubic to spherical. The number of prismatic loops around the dispersoids will be reduced if the number of vacancy type prismatic loops is less than of interstitial type, also reducing η. Hence the value of η is expected to be smaller than unity. In absence of dynamic recovery, the total GND density formed around all the dispersoids equals

$$\rho_G^+ = \int_0^\infty \frac{24\eta r^2\gamma}{b}\varphi dr\,. \quad (6)$$

Here φ is the dispersoid size distribution (number of dispersoids per radius and per volume). The geometric slip length is defined as

$$\lambda = \left(12\eta\int_0^\infty r^2\varphi dr\right)^{-1}. \quad (7)$$

The storage rate corresponding to Eq. (6) and (7) is

$$\frac{d\rho_G{}^{+}}{d\gamma} = \frac{2}{b\lambda}. \tag{8}$$

The calculation of λ requires the dispersoid size distribution. The slip length λ is usually formulated as a simple function of the mean radius and the volume fraction of dispersoids, assumed to be monodisperse. However, the measured distributions and Eq. (7) provide a better estimate. The dispersoid size distributions of BH fit a lognormal distribution well, while BL fit a Γ-distribution well [article 1]. The fitted distribution functions were used to calculate λ with a threshold diameter of 40 nm. The threshold diameter is chosen due to the limit resolution of SEM measurement, but it affects the calculation little. The values of λ are $2.3\eta^{-1}$ μm for BH and $3.5\eta^{-1}$ μm for BL.

The GNDs will experience dynamic recovery as the number of prismatic loops increases. In our work the dynamic recovery of the GNDs in the form of prismatic loops is treated in a simple approach, where the evolution equation of GND density is formulated similar as Eq. (4):

$$\frac{d\rho_G}{d\gamma} = \frac{2}{b\lambda}\left(1-\frac{\rho_G}{\rho_{G,S}}\right). \tag{9}$$

Here $\rho_{G,S}$ is the saturation level of the GND density per total material volume. This quantity depends on the dispersoid size distribution. This approach implies that the dynamic recovery of GNDs is assumed to follow a somehow similar mechanism as forest dislocations. An analytical solution of Eq. (9) is

$$\rho_G = \rho_{G,S}\left(1-\exp\left(-\frac{2\gamma}{b\lambda\rho_{G,S}}\right)\right). \tag{10}$$

As in Ashby's theory the density ρ_G has so far been treated as a global dislocation density, i.e. the sum of the GND lengths per total considered material volume. A more detailed approach should take into account that the prismatic loops are stored in certain regions around each dispersoid. With octahedral slip the glide planes of the prismatic loops for a considered dislocation can only be those of the two co-directional slip systems of its Burgers vector. The glide plane of the loops will be parallel to the direction of the Burgers vector, i.e. the loops will ideally glide along a cylinder of radius

approximately similar to the dispersoid radius and in the direction of the Burgers vector of the dislocation. This also holds if non-octahedral glide in the cube planes occurs, i.e. {100}<110> slip systems are activated locally. The prismatic loop formed first is the furthest from the dispersoid [6] and the distance it glides increases with strain and depends on how many loops that follows behind. Reaching a certain distance away from the dispersoid the loops start interacting with neighboring dispersoids. Therefore the third dimension of the GND zones is not related directly to dispersoid dimensions but to this interaction distance, i.e. the GND zone volume for one prismatic loop direction equals $\pi r^2 l_p$, where l_p is the interaction distance. Ashby [7] used the linear separation of particles, $l_p \approx 4r/(3f_d)$, where f_d is the volume fraction of dispersoids, in his stability estimate, assuming a pile up towards the first particle the chain of prismatic loops hits. An objection to Ashby's estimate can be made, namely that the other particle that is being hit will be bypassed by dislocations of the same slip system and consequently omit prismatic loops with the same Burgers vector gliding in the opposite direction and with opposite dislocation direction. These will enhance dynamic recovery. One of these opposite chains of loops will be of vacancy type, and decohesion at the dispersoid surface may occur. In both cases the other dispersoid will not act entirely as a barrier but also as a dislocation annihilation source. Furthermore, Ashby's estimate implies that the sum of the volumes occupied by the "cylinders" of prismatic loops will add up to a volume equal to the entire material volume when counting only one single set of interstitial type prismatic loops in one direction per particle. In multiple slip many "cylinders" of prismatic loops will then overlap, i.e. the prismatic loops emitted from one particle will interact with prismatic loops from one of the closest neighboring particles much earlier than hitting another particle. The relevant length scale for this to occur is the average distance between neighboring particles, which for randomly uniformly dispersed spherical particles equals

$$l_p \sim \left(\frac{4\pi}{3f_d}\right)^{\frac{1}{3}} r. \qquad (11)$$

If this limits the volume fraction of GND zones, then $\pi r^2 l_p n_c n_s$ is the maximum volume of GNDs corresponding to a dispersoid, where n_s is the number of activated slip systems

per grain, and n_c is the number of GND columns for each activated slip system (n_c=1 or 2). Then this volume is used as a constant for the evolution of GND density. For the case of spherical particles, the volume fraction of GNDs, f_g, scales with the dispersoid volume fraction, f_d, as follows

$$f_g = \frac{\pi r^2 l_p n_c n_s}{4\pi r^3 / 3} f_d . \tag{12}$$

By direct application of Eq. (11) to Eq. (12), the scaling relationship is derived as

$$f_g \approx 1.2 n_c n_s f_d^{2/3} = n_g f_d^{2/3} \tag{13}$$

Generally both vacancy and interstitial loops are formed in a slip system (n_c=2), and Taylor model predicts that at least five independent slip systems are activated (n_s~5). Thus, n_g is ~12. However, n_g will be tuned to fit the modeling curve to the experimental curve. The relationship between global GND and local GND density, ρ_g^L, is $\rho_g = f_g \rho_g^L$. The local GND saturation density, $\rho_{g,s}^L$ is assumed to equal the saturation density of forest dislocations. Thus, the global GND saturation density is

$$\rho_{g,s} = f_g \rho_{g,s}^L = n_g f_d^{2/3} \rho_s , \tag{14}$$

The essential assumption of the modeling is that the evolutions of forest dislocations and GNDs are independent. The material is treated as a composite of GND zones and single-phase matrix. This assumption will be further discussed in next section. Earlier TEM studies [15, 21] reported no significant influence of dispersoids on forest dislocation densities. The forest dislocation densities were similar, in the order of 10^{13}m^{-2}, no matter the density of dispersoids are high [21], or low, like AA1050 and AA3207 [15].

The flow stress contribution from the GNDs is

$$\sigma_g = M \alpha G b \sqrt{\rho_g^L} . \tag{15}$$

The total isotropic stress, including GNDs and forest dislocations, is modeled by

$$\sigma_i = f_g \sigma_g + (1 - f_g)\sigma_f . \tag{16}$$

BL contains PFZs, so the calculation of f_g should include the PFZ fraction, i.e. $f_g = f_g^{'}(1 - f_{PFZ})$, where f_g' is calculated using the measured volume fraction in the

dispersoid-containing part of the alloy. There are now six parameters: $\sigma_{b,s}$ and k_b for the internal stress, k and ρ_s for the forest dislocations, n_g for the GND storage, and one more parameter η related to the slip length restrictions. The initial dislocation density ρ_0 was set as zero since it is negligible compared to ρ_s. The model, i.e. Eq. (1)-(3), (5), (7), and (10), was fitted to the experimental σ-σ_y curves of BH and BL. The 0.2% yield stress is used in experimental curves, and 0.2% is also used as the offset of the modeling curves. The fitted values of the parameters are listed in Table 2. The model is capable of fitting the experiments well, as shown in Fig. 3. The modeling is restricted to strains smaller than 0.1, because the Kocks-Mecking approach of isotropic hardening saturates, which leads to a much lower work hardening rate than the experimental curves at strains larger than 0.1. This simple model of the evolution of forest dislocations can be replaced by other models, but the principles of modeling the GNDs and scaling the saturation density of GNDs are shown to give a good approximation.

Table 2. Parameters of the kinematic and isotropic hardening models

	k_b, MPa	$\sigma_{b,s}$, MPa	k, μm^{-1}	ρ_s, μm^{-2}	η	n_g
BH	800	10.4	165	125	0.5	10.5
BL	450	5.7	165	125	0.5	10.5

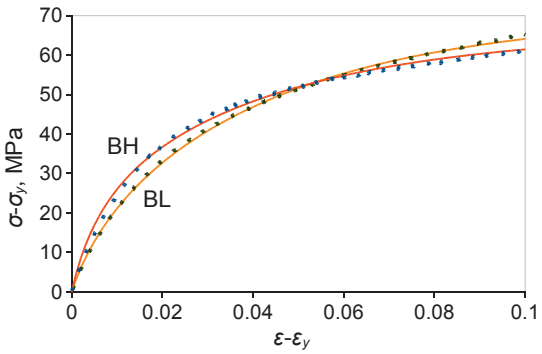

Fig.3 Modeled work hardening curves compared to the experimental curves with a strain offset of 0.2% (lines: modeled; points: experimental).

4. Discussion

A crossover in the work hardening (σ-σ_y) curves was observed at small strains in Fig.3. A similar effect of grain size on stress-strain curves has been reported by Nes and Marthinsen [20], who explained the crossover effect in stress-strain curves from the

Nes's model. Their model accounts for a reduced slip length and enhanced athermal storage of dislocations during stage II. In stage III the model involves a book keeping of how the dislocations are stored in the subgrain interior, in new subgrains and as part of the old subgrain boundaries. It is assumed that the GNDs are mainly stored in the subgrain interior, where they are counted as part of the density of statistically stored interior dislocations. This dislocation density saturates to a constant level and does not contribute to work hardening in stage III. Furthermore, it follows from their book keeping of how the dislocations are stored, that the storage of dislocations as part of building new subgrain boundaries is comparatively decreased, leading to a reduced work hardening in stage III. Hence the crossover is, according to their model, directly related to the transition from stage II-III. The model proposed here is simpler and not directly related to this transition.

The modeling presented in section 3 fits well the work hardening curves at small strains, indicating that the model can describe the work hardening behavior. Figure 4 shows that the predicted density of GNDs increases much faster than that of forest dislocations at the initial deformation, and they dominate before the saturation. After the saturation, the local density of GNDs can not increase any more. Thus, it is reasonable to neglect the forest dislocations in GND zones (f_g) in the model. The generation of GNDs due to the presence of dispersoids results in a high work hardening rate at the very beginning but soon also a strong dynamic recovery. The GND density saturates at a small strain, and the work hardening rate subsequently depends approximately on the forest dislocation density as:

$$\frac{d\sigma}{d\varepsilon} = (1 - f_g)\frac{d\sigma_f}{d\varepsilon}. \qquad (17)$$

After the saturation of GNDs, a large f_g leads to a reduced work hardening rate according to Eq. (17). This explains the influence of dispersoids on work hardening.

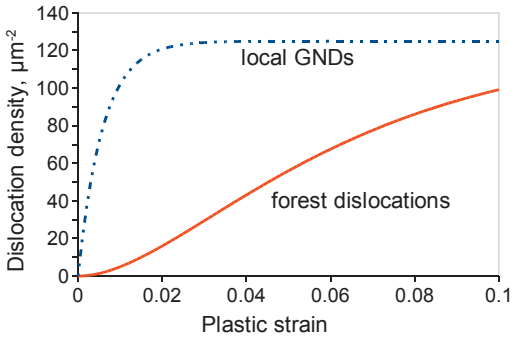

Fig. 4 The local densities of geometrically necessary dislocations (GNDs) and forest dislocations in BH from modeling.

The storage of forest dislocations is assumed to be independent of the dispersoid density and depends only on the forest dislocation density, in the present model as in others [13-14]. The model without σ_b nor ρ_g, i.e. only Eq. (3) and (5), with the same parameters was applied to the experimental curve of an Al-Mn alloy containing a similar solute content by Ryen et al. [22]. Note that the solute content of Ref. [22] was recalculated based on the measured electrical conductivity, using the same procedure as here. The Al-Mn alloy in [22] contained coarse particles but very few dispersoids. Hence the storage of prismatic loops around the dispersoids can be neglected in the alloy. The experimental σ-σ_y curve is comprised of forest hardening but also a contribution from the internal stress due to the constituent particles. The difference between the two curves in Fig.5 should be identical to the internal stress. The modeling curve has a similar work hardening rate to the experimental curve at strains larger than 0.06, suggesting that the fitted parameters work reasonably well also for this case.

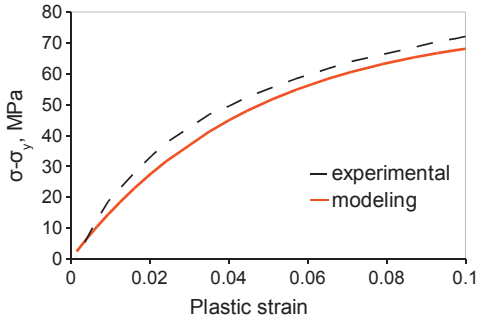

Fig. 5 The modeled forest hardening compared to the experimental curve of an Al-Mn

alloy from [22].

5. Conclusions

It is found that a high density of non-shearable dispersoids causes an increased initial work hardening followed by a reduced work hardening at strains beyond 5%. The explanation of the reduced hardening beyond a certain strain is that the local dislocation density saturates and does not contribute to further work hardening in the volume fraction of the material containing the GNDs. A new mathematical model has been suggested with an additional evolution equation for the GND density using the measured particle distributions as input. In the model an estimate for the volume fraction of the GNDs is made based on that loops emitted from adjacent particles interact and enhance the dynamic recovery of prismatic loops so that their interaction distance scales with the average distance between the neighboring particles. The model has been quantitatively tested for dispersoids in an Al-Mn alloy but should be applicable to other alloys containing non-shearable particles of similar size.

Acknowledgements
The work is funded by the Research Council of Norway, Hydro and Sapa Technology under the MOREAL project.

References

[1] M.F. Ashby, Philos. Mag., 14 (1966) 1157-1178.
[2] J.D. Embury, W.J. Poole, D.J. Lloyd, Mater. Sci. Forum, 519-521 (2006) 71-78.
[3] M.H. Lewis, J.W. Martin, Acta Metall., 11 (1963) 1207-1214.
[4] P. Hirsch, F. Humphreys, Proc. R. Soc. London, A, 318 (1970) 45-72.
[5] F. Humphreys, P. Hirsch, Proc. R. Soc. London, A, 318 (1970) 73-92.
[6] F.J. Humphreys, A.T. Stewart, Surf. Sci., 31 (1972) 389-421.
[7] M.F. Ashby, The Deformation of Plastically Non-homogeneous Alloys, in: A. Kelly, R.B. Nicholson (Eds.) Strengthening Methods in Crystals, Elsevier, Amsterdam, 1971, pp. 137-192.
[8] M.F. Ashby, Philos. Mag., 21 (1970) 399-424.
[9] V. Gerold, Precipitation hardening, in: F.R.N. Nabarro (Ed.) Dislocations in solids, North-Holland, New York, 1979, pp. 219-260.
[10] L.M. Brown, W.M. Stobbs, Philos. Mag., 23 (1971) 1185-1199.
[11] L.M. Brown, W.M. Stobbs, Philos. Mag., 23 (1971) 1201-1233.
[12] H. Proudhon, W.J. Poole, X. Wang, Y. Bréchet, Philos Mag, 88 (2008) 621-640.
[13] J. da Costa Teixeira, L. Bourgeois, C.W. Sinclair, C.R. Hutchinson, Acta Mater., 57 (2009) 6075-6089.
[14] G. Fribourg, Y. Bréchet, A. Deschamps, A. Simar, Acta Mater., 59 (2011) 3621-3635.

[15] B. Forbord, K. Marthinsen, E. Nes, Mater. Sci. Forum, 331-337 (2000) 557-564.
[16] O.R. Myhr, Ø. Grong, K.O. Pedersen, Metall. Mater. Trans. A, 41 (2010) 2276-2289.
[17] M. Okabe, T. Mori, Acta Metall., 27 (1979) 1373-1380.
[18] K. Matsuura, Acta Metall., 29 (1981) 643-650.
[19] Y. Estrin, H. Mecking, Acta Metall., 32 (1984) 57-70.
[20] E. Nes, K. Marthinsen, Mater. Sci. Eng., A, 322 (2002) 176-193.
[21] C.Y. Barlow, N. Hansen, Y.L. Liu, Acta Mater., 50 (2002) 171-182.
[22] Ø. Ryen, O. Nijs, E. Sjölander, B. Holmedal, H.E. Ekström, E. Nes, Metall. Mater. Trans. A, 37 (2006) 1999-2006.

Article 3

Comparison of the influence of Si and Fe in 99.999% purity aluminum and in commercial purity aluminum*

Qinglong Zhao, Marius Slagsvold, Bjørn Holmedal
Department of Materials Science and Engineering, Norwegian University of Science and Technology, Trondheim N-7491, Norway

Abstract: It is found that in tensile tests 99.999% purity aluminum with additions of about 0.1wt% Fe and Si is similar to commercial 99.8% purity aluminum, suggesting that the strength and work hardening is controlled by Fe and Si, i.e. that the other trace elements play a minor role.

Keywords: aluminum; plastic deformation; mechanical properties

It is well known that commercially pure aluminum has higher strength and work hardening than high-purity aluminum. The same trend of increasing strength with decreasing purity can be seen when comparing commercially pure aluminum of various purities [1]. A previous review [2] demonstrates that a higher purity of the aluminum leads to a lower critical resolved shear stress of single crystals and a lower yield strength of polycrystals. The strengthening of high-purity aluminum is different from that in commercially pure aluminum in several ways. The grain size dependency of the yield stress is stronger, i.e. the Hall-Petch relationship in 99.999% Al is different from those in 99.5% Al [3]. It has been reported that the solid solution strengthening and work hardening in commercial purity base alloys are stronger than in high-purity base binary alloys with Mn or Mg in solid solution [4-5]. In high-purity aluminum the impurities can significantly influence the strength, e.g. in the hot compression experiments [6] a 99.99% Al had a higher flow stress than a 99.999% Al at high strain rates. However, it is not clear which elements play a major role among the dozens of trace elements. Iron and silicon are the main impurities in commercial aluminum. They

* NOTICE: this is the author's version of a work that was accepted for publication in *Scripta Materialia*. A definitive version was published in *Scripta Materialia 67(2012) 217-220*, DOI: 10.1016/j.scriptamat.2012.04.023

come from the smelting process and will accumulate during recycling of unsorted scrap metal, where they are difficult to eliminate. Their influence on the hardening of commercially pure Al is of primary interest and is investigated in this work.

Few experimental results on the strength of Al-Fe binary alloys are reported so far, probably since the solubility of Fe in Al is very low and the Si-impurity is difficult to eliminate. Research on Al-Fe-Si alloys is often reported instead of on Al-Fe binary alloys. Diak et al. [7] studied the strain rate sensitivity of Al-Fe alloys, but actually the Si atomic concentration was no less than Fe. Mahon and Marshall [8] reported on the effect of the solutes Fe and Si on yield stress in "super purity binary alloys", but the purity of their metal was not specified.

Three aluminum variants are studied in this paper: a 99.999% high-purity base metal (HP), a commercial-purity base (CP) and a high-purity ternary alloy (HA) with Fe and Si added to the HP base metal to reach similar amounts as in the CP base. The materials were DC casted by Hydro Aluminum in Bonn, all of them in exactly the same manner and without using a grain refiner. The nominal compositions of the materials are listed in Table I. The concentrations of the trace elements in the high-purity base were less than 1ppm individually. The trace elements in the commercial-purity base (CP) were less than 50ppm individually, except Ga and V (about 90ppm each). The materials were homogenized at 600°C for 8 hours and later extruded at 460°C into flat profiles being 70mm wide and 5mm thick. The extrusion profiles were cold rolled to 1mm thickness in 4 passes (reduction 80%). The rolled sheets were annealed for half an hour to recrystallize. Proper recrystallization temperatures for the three considered qualities were determined from a series, where the hardness was measured subsequent to annealing at various temperatures. The recrystallized grain sizes were measured by optical microscopy and are listed together with the recrystallization temperatures in Table I.

Table I. The nominal compositions (mass ppm except Al in wt%), recrystallization temperatures and grain sizes

Al	Fe, ppm	Si, ppm	Other elements, ppm	Annealing temperature, ºC	Grain size, µm

HP	99.999%	0.72	1.07	7.79	350	167
HA	99.865%	660	680	8.70	375	27
CP	99.799%	940	690	382.2	375	30

The solute contents of the elements Fe and Si were measured by JEOL JXA-8500F electron probe micro-analyzer (EPMA). The constituent particles containing Fe and Si were observed by back-scattered electron imaging at 15KV in a field emission gun SEM Zeiss Ultra 55 with an EDS and an EBSD detector. The textures were measured by coarse step EBSD mapping of 2~3mm^2 areas orthogonal to the transverse sheet direction.

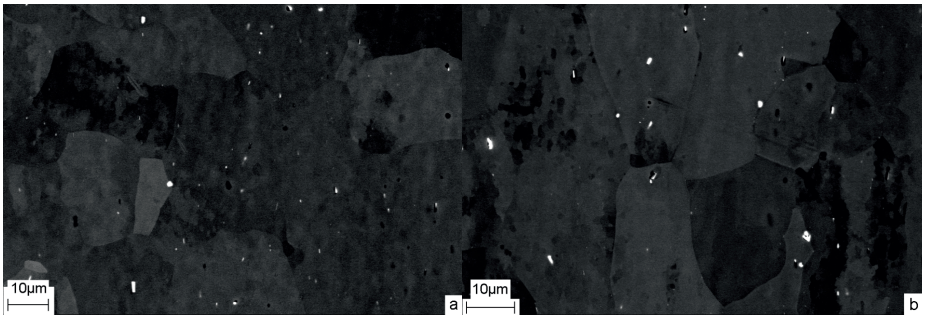

Figure 1. SEM micrography of constituent particles in a) HA and b) CP

Tensile specimens were machined from the recrystallized sheets with 25mm wide and 64mm long parallel sections. The tensile axis was along the rolling direction. An MTS 810 hydraulic testing machine was run under a constant ramp rate at room temperature, giving a nominal strain rate of $10^{-3}s^{-1}$. The yield strength (0.2% offset, Rp02), and the ultimate tensile strength (UTS) were measured according to ASTM E8M-09.

Table II. The solute concentrations in solid solution, particle mean radiuses and area fractions, and the strengths at a true strain rate of $10^{-3}s^{-1}$

	Fe in solution, wt%	Si in solution, wt%	Particle radius, µm	Particle area fraction, %	Orowan shear stress, MPa	Rp02, MPa	UTS, MPa
HP	0.00007	0.00011	-	-	-	12.4	41.6
HA	0.026	0.049	0.31	0.09	0.6	25.6	73.2
CP	0.025	0.053	0.36	0.08	0.5	25.8	72.7

The measured Fe and Si solute levels were very similar in both HA and CP (Table II). The Fe concentration in solution was about 0.026wt%, and Si 0.05wt%. The 5N high-purity aluminum (HP) was single phase, while HA and CP contained some particles. The compositions of the particles were measured by EDS, giving the atomic ratio of

Fe/Si to be 0.3~1. Thus, the particles were probably β-AlFeSi according to Al-Fe-Si ternary phase diagram [9]. The size distributions of the constituent particles were characterized by SEM. The particle distributions were very similar in HA and CP (Figure 1). The particle size distributions fitted well log-normal distribution functions (Figure 2). The average radiuses of the particles were very similar in both alloys (Table II). The contributions from particles to the strength can be calculated by the Orowan shear stress equation.

$$\tau_{Oro} = \frac{0.81Gb\ln(2r_s/b)}{2\pi\sqrt{1-\nu}(L_s-2r_s)},\ L_s = r\left(\frac{2\pi}{3f}\right)^{1/2},\ r_s = \frac{\pi r}{4}$$

This equation was given by Brown and Ham [10], and was discussed by Ardell [11]. The results are listed in Table II, with the assumption that the shear modulus G=26GPa, the Poisson's ratio $\nu = 0.35$, the Burgers vector $b = 0.286$nm and that the shape of particles is spherical. Based on the measured area fraction of particles f and their average radius r in Table II, the Orowan shear stresses were calculated to be very small (~0.5MPa) and can be neglected compared to the yield strength.

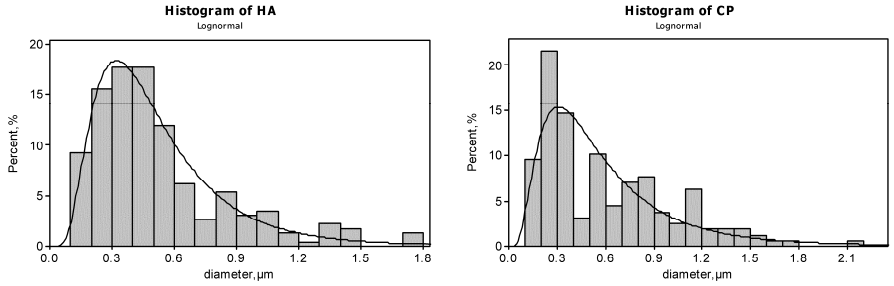

Figure 2. The size distributions of particles in HA and CP (histograms), and the fitting of log-normal distributions (solid lines)

The recrystallization texture of HA and CP consisted of strong Goss {110}<001> and Cube {100}<001> components, and other weak texture components (e.g. retained rolling texture components), as shown in Figure 3. The textures of all the investigated variants were comparable and the calculated Taylor factors for tensile tests in the rolling direction were about 2.7 for all three variants.

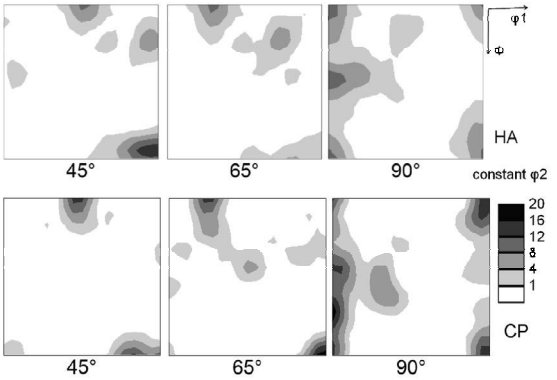

Figure 3. Selected ODF sections of a) HA and b) CP, showing the textures after recrystallization

The stress-strain curves of HA and CP were very similar and significantly above those of HP, as shown in Figure 4. Also their work hardening rates were higher than that of the pure aluminum HP. Their yield strength and UTS (see Table II) were similar to those of a fully softened commercial 1080A alloy [1], confirming that the two variants (HA and CP) behave as a typical commercially pure aluminum. HA and CP had significantly smaller grains than HP, where their smaller grain size also contributes to their higher strength. Hansen [3] investigated the Hall-Petch relation in a similar 99.999% pure aluminum, where one of his specimens had similar grain size as HA and CP, and another had similar grain size as HP. These stress-strain curves from [3] are included in Figure 4. The decrease of the grain size from 170μm to 34μm increased the work hardening and the yield strength (about 2MPa). The curve labeled 170μm is almost similar to HP, where the small difference may be due to slightly different texture and chemistry. The curves of HA and CP are far above Hansen's curve with similar grain size (34μm), suggesting that the significant hardening difference are contributed by Fe and Si solutes.

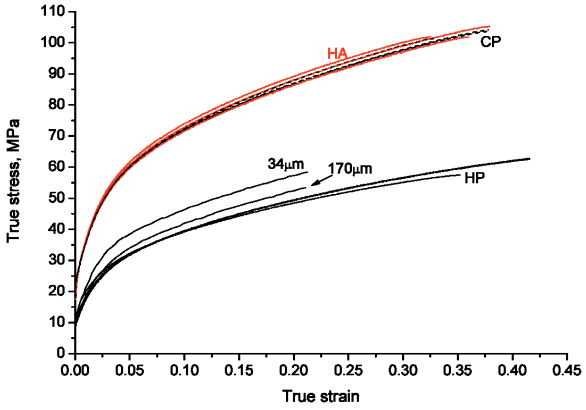

Figure 4. Stress-strain curves of HP, HA and CP at a strain rate of $10^{-3}s^{-1}$, and the curves of 99.999% aluminum with grain sizes of 34μm and 170μm from [3].

The additional stress caused by the solute concentration of element i, c_i, can be described by the equation $\Delta\sigma_i = Hc_i^n$, where H and n are specific for the considered element. According to reference [12] multi-component solid solution hardening can be estimated from the contribution from each element by the equation $\Delta\sigma = \sum_i \left(\Delta\sigma_i^{1/n}\right)^n$, assuming a random distribution of the solute atoms. Based on the data from reference [8] an estimate of the solute contribution in HA is 6.3MPa (n=1/2, Friedel statistics) or 6.8 MPa (n=2/3, Labusch statistics), which in both cases are evidently smaller than the actual contribution, i.e. about 10MPa, which is the difference between HA and the high-purity aluminum with 34μm grain size[3]. Thus, it is plausible that impurity hardening is contributed not only by Fe and Si individually, but also by a synergy effect between the Fe and Si solutes. More investigations of solid solution hardening in high-purity Al-Fe and Al-Si binary alloys are required to clarify the effect of Fe and Si in future works.

Even though HA and CP contain similar amounts of Fe and Si, their impurity levels differ significantly. Still the stress-strain curves of CP are the same as those of HA, indicating that the contribution from the other impurities is negligible. Nearly half of the impurity in CP is Fe, from which a major fraction is in the particles and does not contribute much to the hardening. The number of impurity atoms in CP left behind if

excluding Fe and Si is considerable higher than the number of Fe atoms in solid solution. The solid solution concentrations of both Fe and of Si are similar for CP and HA and in sum they outnumber the other impurity atoms. The power law nature of the solute hardening contributions is very steep at small concentrations as compared to larger concentrations; hence the effect of adding impurities to a commercial base is much smaller than adding them to a high purity quality. The distribution and impact of the other impurity elements are not known but it can be concluded that the major contribution comes from Fe and Si in solid solution.

In conclusion, the impurity hardening in 99.8% commercially pure aluminum can be obtained by additions of only Fe and Si into a 99.999% high-purity base metal, and then the contribution from the other trace impurities is negligible. The strength and work hardening of an investigated high-purity based ternary, dilute Al-Fe-Si alloy were found to be identical to a commercially pure 99.8% aluminum containing similar levels of Fe and Si in solid solution but in addition containing about 0.04% of other impurities. This ternary alloy was significantly stronger than its 99.999% high-purity base metal processed and tested under the same conditions.

Acknowledgements
This work is funded by Research Council of Norway, Hydro and Sapa under the project MOREAL.

References
[1] C.J. Smithells, E.A. Brandes, G.B. Brook, Smithells light metals handbook, Butterworth-Heinemann, Boston, Mass., 1998.
[2] R.P. Reed, Cryogenics, 12 (1972) 259-291.
[3] N. Hansen, Acta Metall., 25 (1977) 863-869.
[4] Ø. Ryen, O. Nijs, E. Sjölander, B. Holmedal, H.E. Ekström, E. Nes, Metall. Mater. Trans., A37 (2006) 1999-2006.
[5] O.D. Sherby, R.A. Anderson, J.E. Dorn, J. Metals, 3 (1951) 643-652.
[6] Y. Prasad, S. Sasidhara, Hot working guide: a compendium of processing maps, ASM International, Materials Park, OH, 1997.
[7] B.J. Diak, S. Saimoto, Mater. Sci. Eng., A234-236 (1997) 1019-1022.
[8] G.J. Mahon, G.J. Marshall, JOM, 48 (1996) 39-42.
[9] V. Raghavan, JPED, 30 (2009) 184-188.
[10] L.M. Brown, R.K. Ham, Dislocation-particle interactions, in: A. Kelly, R.B. Nicholson (Eds.) Strengthening Methods in Crystals, Elsevier, Amsterdam, 1971, pp. 9-135.

[11] A.J. Ardell, Yielding in crystals containing finite dispersed obstacles, in: R.W.C. K.H. Jürgen Buschow, et al (Ed.) Encyclopedia of materials : science and technology, Elsevier, Amsterdam, 2001, pp. 9842-9854.
[12] L.A. Gypen, A. Deruyttere, J. Mater. Sci., 12 (1977) 1028-1033.

Article 4

The effect of silicon on the strengthening and work hardening of aluminum at room temperature*

Qinglong Zhao, Bjørn Holmedal

Department of Materials Science and Engineering, Norwegian University of Science and Technology, Trondheim N-7491, Norway

Abstract: Solution hardening of Al-Si alloys at room temperature was investigated by tensile tests of several aluminum alloys containing various amounts of Si in solution but fabricated from the same commercially pure base material. It is found that Si has a weak strengthening effect but a significant impact on the work hardening. The strengthening was found to be very sensitive to water quenching, which enhances the solute strengthening. Despite the low strengthening effect, the Portevin-Le Chatelier effect was clearly observed during the tension of an alloy containing 0.4 at% Si, suggesting the occurrence of dynamic strain ageing due to surprisingly low levels of Si in solid solution.

Key words: aluminum alloys, mechanical characterization, mechanical properties, Portevin-Le Chatelier effect, solid solution hardening

1. Introduction

Non-heat-treatable aluminum alloys including AA1xxx (commercially pure aluminum), AA3xxx (Al-Mn) and AA5xxx (Al-Mg) systems are widely used in the applications requiring a low to medium strength, a good formability and a good corrosion resistance. Non-heat-treatable alloys owe their strength to the elements in solution, so solid solution hardening is an important strengthening mechanism in such alloys. Furthermore, the solute influence on the work hardening is important when it comes to formability. This is also the case for solution treated 6xxx alloys, where Si and Mg are the major elements in solution. In the commercial alloys a mix of elements are present in solid solution. The ultimate goal is to make models that can handle their complex

* NOTICE: this is the author's version of a work that was accepted for publication in *Materials Science & Engineering A*. A definitive version was published in *Mater. Sci. & Eng. A563(2013) 147-151*, DOI: 10.1016/j.msea.2012.11.062

interplay, and the natural starting point is the investigation of these elements one by one. Our understanding can be improved by atomistic simulations of atom core effects, such as those recently reported in [1-2].

The solute strengthening mechanism has been subjected to investigations for many years. The development of theories and many experimental results have been reviewed by several authors [3-5]. Mg and Mn have generally attracted more attention compared to other elements in aluminum, and studies on both high purity and commercial purity alloys have been reported [6-7]. Small amounts of Si usually exist in most commercial wrought aluminum alloys. Some of the Si atoms form constituent particles with Fe and also precipitate with other elements during heat treatments, while the remaining Si atoms are in solid solution. Hot deformation experiments of commercially pure Al-Si alloys [8] and theoretical calculations [1-2] indicate that Si has a weak solution hardening effect. However, few experimental results have been reported on cold deformation of aluminum containing various contents of Si in solution.

The Portevin-Le Chatelier (PLC) effect, which manifests itself as serrated flow and negative strain rate sensitivity, affects ductility and formability and has been extensively studied [9], especially in Al-Mg alloys. The PLC effect is associated with interaction of diffusing solute atoms with mobile dislocations, known as dynamic strain ageing (DSA). The PLC effect has been observed in Al-Si alloys containing 3-12wt% Si at strain rates between 10^{-4} and $10^{-2}s^{-1}$ at room temperature [10-11]. In Ref. [11] the quenched-in vacancies were suggested to be the governing factor of PLC effect and the PLC effect was claimed to occur also in an Al-0.2wt% Si binary alloy, but no results were shown for alloys with less than 3 wt% Si [11].

In this work, several aluminum alloys containing various amounts of Si in solution but fabricated from the same commercially pure base material, are investigated to explore the effect of Si on mechanical properties and the occurrence of PLC at room temperature.

2. Experimental

Aluminum alloys with three levels of Si contents were fabricated in the same manner by Hydro aluminum. The raw alloys are labeled as S1, S2 and S5 corresponding to the nominal content of Si (refer to Table 1). All the raw alloys were in the direct chill casting condition with a diameter of 22 cm. The S5 alloy was homogenized in two ways to achieve different levels of Si in solution, labeled as S5a and S5b, respectively. The compositions and homogenization treatments are listed in Table 1. Two sets of materials were prepared by different treatments following homogenization. One set of alloys was quenched into water after homogenization to induce excess vacancies. The other set was cooled in air to room temperature (cooling rate ~45 K/min) after homogenization to avoid inducing excess vacancies. The air cooled alloys were used to study solute strengthening of Al-Si, and the water quenched alloys were used to study the effect of quenching on solid solution hardening. All the materials were left at room temperature before further tests.

The solute concentrations in solid solution were measured by a JEOL JXA-8500F electron probe micro-analyzer (EPMA). The microstructure after homogenization was investigated by both a Zeiss Supra 55 field emission gun scanning electron microscope (FEG-SEM) operated at 15kV and a JEOL 2010 transmission electron microscope (TEM) operated at 200 kV. The tensile tests were performed using cylindrical specimens with a diameter of 6 mm, a gauge length of 25 mm and a parallel length of 35 mm. Three parallel tests were performed for each alloy. An MTS 810 hydraulic testing machine was run under a constant ramp rate at room temperature, giving strain rates of about $10^{-1}s^{-1}$ and $10^{-3}s^{-1}$.

Table 1. The compositions and homogenization treatments

	Al wt%	Nominal Si, wt%	Nominal Fe, wt%	Homogenization	Si in solution, at%
S1	99.73	0.07	0.15	833K 6h	0.03
S2	99.67	0.15	0.14	833K 6h	0.12
S5a	99.29	0.50	0.15	853K 4h +25K/h to 673K 4h	0.34
S5b	99.29	0.50	0.15	833K 6h	0.43

3. Results and discussion

3.1 Microstructure

The concentration of Fe in solid solution was about 0.01at% (measured by EPMA), which to the present work is negligible. The atomic concentrations of Si in solid solution are listed in Table 1. Constituent particles formed at dendrites and grain boundaries during casting and homogenization (Fig.1). The constituent particles are expected to be mainly Fe_4Al_{13} and β-AlFeSi according to the ternary phase diagram [12], and in S5a some Si particles formed during homogenization. The average radius of the constituent particles in all the alloys was ~ 0.7 μm, and the area fractions were ~0.3%. No fine precipitates were observed by TEM in the air cooled S5b, suggesting that no precipitation occurred during cooling. The texture is expected to be random due to the homogeneous cast structure. The grain sizes of the materials except S1 were similar, about 107μm on average. S1 had coarser grains, and the mean diameter was 162μm.

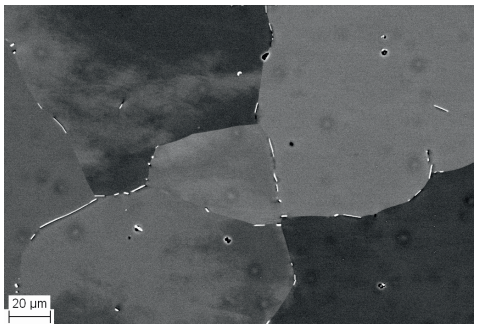

Fig.1 back-scattered electron image of constituent particles in S5b, showing that the coarse particles were distributed mainly at grain boundaries.

3.2 Portevin-Le Chatelier effect in Al-Si

The alloy with the highest amount of Si in solution (S5b) was tested by a strain rate change tensile test to illustrate the occurrence of the PLC effect in this alloy (Fig.2). Both water quenched and air cooled S5b showed similar serrations in the tensile curves. Serrated yielding occurred at the strain rate of $10^{-3}s^{-1}$, showing type A serrations (Fig.2). For a description of the types of serrations, see reference [9]. A segment of the testing curve of S1 is also shown in Fig.2, confirming that the type A serrations are clearly distinguishable from background fluctuations. The increase of the strain rate at a strain of 0.06 to $0.1s^{-1}$ reduced the serrated flow behavior in Fig.2. However, serrated yielding

reappeared (as type D) later at strains slightly larger than 0.1, still at the highest strain rate. However, the serrations became more pronounced when the strain rate was again changed back to $10^{-3}s^{-1}$ at a strain of 0.13. Type A serrations were also observed in S5a, but less pronounced. The presence of the PLC effect confirms that DSA occurs in a dilute Al-Si alloy, and furthermore that the quenched-in excess vacancies in the water quenched specimen did not affect the PLC effect.

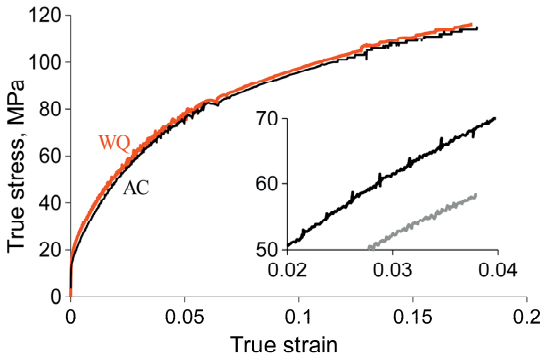

Fig.2 Strain rate change during tensile test of water quenched (WQ) and air cooled (AC) S5b (initially $10^{-3}s^{-1}$, changed to $0.1s^{-1}$ at strain of 0.06, then back to $10^{-3}s^{-1}$ at strain of 0.13). The inserted figure illustrates the beginning of type A serrations with a grey line showing the fluctuations of a test on S1 (the line is shifted to appear in the same range as S5b).

In general DSA is expected in Al-Si alloys, since Si has similar diffusion coefficient as Mg in aluminum [13]. The PLC effect has also earlier been observed in supersaturated Al-Si alloys [10-11]. Early research on Al-1wt%Si alloy wires and ribbons [14] noted that the tensile curves were serrated at room temperature regardless of the quenching rate; whereas the tensile curves tested at 197K were smooth. This observation indicates that the PLC effect is due to DSA. The PLC effect in a dilute Al-Si alloy is demonstrated in Fig. 2. The occurrence of PLC requires the concentration to be larger than a certain critical value. The critical concentration for Al-Mg at room temperature has been estimated to be 0.86 wt%, and accordingly the PLC effect was not observed in an Al-0.45wt%Mg [15]. On the other hand the Al-0.43at%Si alloy (S5b) in this work shows the PLC effect, indicating that Si results in a stronger DSA than Mg. Curtin et al.

[16] demonstrated the cross-core model of DSA for Al-Mg to be mono-atom-hop motion of solutes from the compression to the tension side of the edge dislocation core. A similar mechanism may also be applicable to explain how the DSA occurs in dilute Al-Si alloys. The size misfit of Si in an aluminum matrix is about half of Mg and is of opposite sign [2], hence the atomic jump will be in the opposite direction across the core. The dislocation interactions with solutes Si can be investigated by atomistic simulations and might be different than with Mg.

3.3 The mechanical properties of Al-Si alloys

True stress-strain curves from tensile tests at a strain rate of ~$0.1s^{-1}$ are shown in Figure 3. The flow stresses were almost similar at the initial stage of plastic deformation, but the influence of Si on the flow stress became more significant as the strain increased. The addition of Si increased the ultimate tensile strength (UTS) but decreased the uniform elongation as shown in Table 2.

Table 2 Ultimate tensile strength (UTS) and uniform elongation (UE) of air cooled and water quenched Al-Si alloys.

	Air cooled		Water quenched	
	UTS, MPa	UE,%	UTS, MPa	UE,%
S1	75.7	35	75.3	34
S2	81.5	33	81.7	33
S5a	94.5	29	94.8	29
S5b	98.6	29	99.4	28

The yield strength of the alloys was increased by water quenching compared to the air cooled alloys (Fig.3b), implying that quenched-in vacancies somehow contributed to the strength. However, the stress-strain curves of the water quenched alloy and the air cooled converged at larger strains, so the UTS and uniform elongation were not affected by quenching (Table 2). It suggests that the effect of quenching is restricted to a short transient subsequent to yielding, and quenching does not affect the further work hardening.

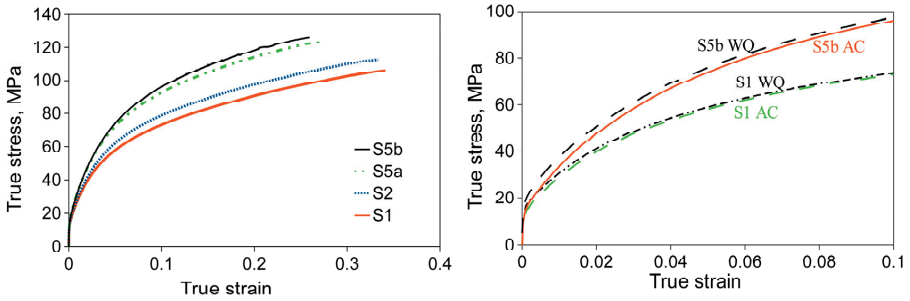

Fig.3 a) Stress-strain curves of air cooled Al-Si alloys from tensile tests at a strain rate of ~0.1s^{-1}. b) Comparison of stress-strain curves of air cooled (AC) and water quenched (WQ) alloys in the initial part of the stress-strain curves.

3.4 Solid solution hardening

Generally the flow stress is affected by the solute content, particles and the grain size. The constituent particles in the present alloys were relatively large and of a small volume fraction and formed at dendrite and grain boundaries. They affect the flow stress to a limited amount. The contribution to the flow stress of the grain size is estimated by the Hall-Petch relation, where a Hall-Petch parameter, k in $kd^{-1/2}$ of k=0.78MPa·$mm^{1/2}$ for 99.5% commercially pure aluminum [17] is used for the calculations. According to these calculations, the difference in yield stress between S1 and the other materials due to the grain size contribution is found to be ~ 0.4 MPa. This small contribution of grain size to the flow stress is negligible and comparable to the experimental errors. The relation between the flow stress and the solute concentration is commonly expressed as:

$$\sigma=\sigma_0+Hc^n, \quad (1)$$

where σ_0 is the flow stress of the pure metal, and H and n are constants. All the materials investigated in this work may be classified as commercially pure aluminum alloys. The value of H at strain of 0.002 indicates the solute effect on the yield strength, while at higher strains H reflects the combination of the solute effect on strength and work hardening. Equation (1) can be used to estimate the solution hardening of Si for a comparison to literature works. The exponent n is in general in the range from 0.5 to 1, and its precise value has been found to be close to 1 for Al-Mg alloys. The value of H in equation (1) for Mg is ~14.3 MPa/at% in both commercially pure [6] and high-purity

aluminum [7] with n=1. For the considered Al-Si alloys, the value of H in equation (1) for air cooled Al-Si is determined to be 7.6 MPa/at% and σ_0 is 16.2 MPa, using n=1. The strengthening effect of Si is thus nearly half that of Mg in aluminum at room temperature. The value of H for the water quenched Al-Si alloys is determined to be 12.6 MPa/at% (with σ_0=19.6 MPa). If quench hardening is independent of solid solution hardening, the value of H would not be affected by the quenching. The difference in the values of H between the air cooled alloys and the water quenched ones suggests that the strengthening effect of quenching is enhanced by the solutes, implying that solutes interact with quenched-in vacancies.

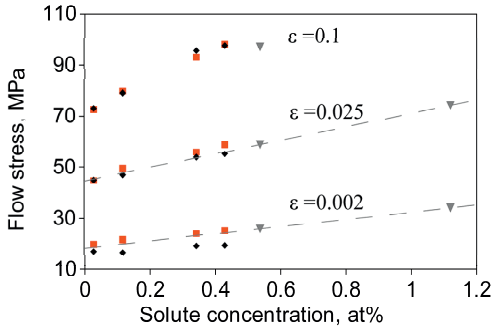

Fig. 4 Flow stress as a function of solute concentration at various strains. ■: water quenched Al-Si alloys; ◆: air cooled Al-Si alloys; ▼: Al-Mg alloys from Ref. [6] , and linear trend lines are included for Al-Mg (dashed lines).

The flow stress of the air cooled and water quenched Al-Si alloys in this work and Al-Mg alloys from ref. [6] at various strains is plotted as a function of the atomic concentration of solutes in Figure 4. The Al-Mg alloys in ref. [6] had similar contents of Si and Fe as S1 in this work. Linear trend lines of Al-Mg are also plotted in Figure 4. It should be noted that the Al-Mg alloys [6] were tested at a strain rate of ~$10^{-3}s^{-1}$. It has been reported that the yield strength of Al-Mg alloys is affected weakly by strain rates below $10s^{-1}$, and that the yield strength at the strain rate of $0.1s^{-1}$ was no stronger than those at lower strain rates [7]. Hence, the different strain rates should not affect much the comparison of Al-Si and Al-Mg. The 0.2% yield stresses of air cooled Al-Si are below the linear trend line of Al-Mg (the dashed line in Fig.4), suggesting that the influence of Si on solution hardening is weaker than of Mg. However, the flow stresses

of Al-Si fit well the same trend line of Al-Mg at a strain of 0.025, suggesting the flow stress of Al-Si is no lower than Al-Mg at larger strains. This indicates that Si has a stronger effect than Mg on the work hardening. The comparison between water quenched and air cooled alloys in Fig. 4 confirms that the quench hardening contribution vanishes as the strain increases.

The solid solution hardening arises due to the strain fields from the solute atoms in the matrix, and the strain field is related to the size misfit and modulus misfit. The size and modulus misfits of Si are about half of the values of Mg [18], so the hardening effect of Si has been theoretically predicted using first-principles atomistic calculations to be much weaker than Mg, less than half of that of Mg at low temperatures [2]. The concentration dependence of solute strengthening can be estimated from the classical theories (Labusch or Friedel). At higher temperatures, the temperature dependence has to be considered. The energy barrier of Si for dislocations is predicted to be smaller than that of Mg [2], suggesting that the decrease of the hardening effect of Si with increasing temperature is more rapid than that of Mg. Thus, the solution hardening of Si atoms in theory should be much weaker than that of Mg atoms at room temperature. The stress contribution by solution hardening, $\Delta\sigma_s$ at elevated temperatures can be calculated from the model in ref. [2]. The values of $\Delta\sigma_s$ at 290K are calculated to be 2.2 MPa for S5a, and 2.8 MPa for S5b. The experimental differences between the yield strength and σ_0 in equation (1) are 3.0 MPa for S5a, and 3.2 MPa for S5b. The model predictions are thus in good agreement with the measurements.

3.5 Work hardening

The work hardening rates $d\sigma/d\varepsilon$ at strains of 0.01 and 0.1 of Al-Si and Al-Mg [6] are plotted in Figure 5. The values of work hardening rates of Al-Si at a strain of 0.01 are above the trend line for Al-Mg, suggesting that Si has a stronger effect than Mg on the work hardening. As a consequence the Al-Si and the Al-Mg strengths are very similar at a strain of 0.025 in Fig. 4, although the initial strength of Al-Si was much weaker than Al-Mg. Also at a strain of 0.1 the effect of Si on work hardening remains similar as for Al-Mg.

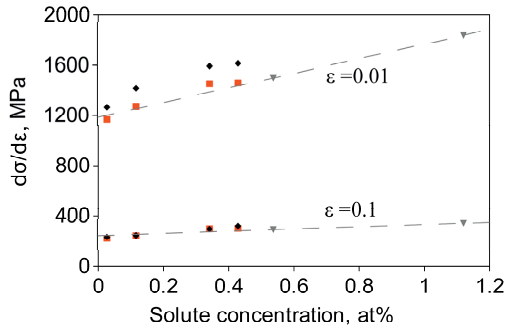

Fig.5 Work hardening rates as a function of solute concentrations at various strains, suggesting that solutes increase work hardening rates. ■: water quenched Al-Si alloys; ◆: air cooled Al-Si alloys; ▼: Al-Mg alloys from Ref. [6], including linear trend lines for Al-Mg.

Work hardening is a result of dislocation storage and their dynamic recovery. The strain rate does not affect evidently the athermal storage of dislocations, but affects dynamic recovery significantly [19-20]. The tensile tests of Al-Mg at various strain rates in [21] indicates that DSA enhances the work hardening by a lower dynamic recovery at small strain rates. A possible explanation for this is suggested based on a simplistic picture of dynamic recovery events occurring as annihilations of dipole configurations [19], where opposite dipole segments have to move a distance equal to the dipole spacing in order to annihilate. Their movement would in general also involve cross slip or climb, which might be differently influenced by the Si solutes than the glide of mobile dislocations. The energy barrier of the dipole segment movement decreases with the decreased dipole spacing. Thus, the velocity of the dipole segment increases with the decreased dipole spacing. At early stage of deformation, the average dipole spacing is large due to low dislocation density. The velocity of the dipole segment might be sufficiently small that the dipole movement is subject to DSA, i.e. it is more effectively dragged by solute atoms than the glide of mobile dislocations. Thus, a strong DSA effect weakens the dynamic recovery and increases the work hardening. It explains the initial increased work hardening rate in Al-Si as compared to Al-Mg [6] by the stronger DSA effect of Si in aluminum. As strain increases, the average dipole spacing decreases due to the increased dislocation density. Hence such segments move with an increased speed so

that the DSA effect is not effective. At larger strains (≧~0.1), the dependency of work hardening on the solute level is similar for Al-Si as for Al-Mn and Al-Mg [6].

4. Summary

Si in aluminum has a weak strengthening effect at room temperature, but increases the work hardening significantly at strains below 0.1. Quenching increases the yield strength of Al-Si alloys, but its effect diminishes as strain increases and does not affect the flow stress and work hardening at strains larger than 0.1. The dependency of strengthening on the solute level in water quenched Al-Si alloys is stronger than that in air cooled alloys, implying that Si solutes interact with quenched-in vacancies. It requires further investigations to clarify the mechanism of such interactions. The occurrence of PLC in a dilute Al-Si alloy is confirmed in the present work. Quenching does not affect the PLC effect. It is suggested that DSA retards the dynamic recovery at small strains, causing an enhanced initial work hardening. DSA involves dislocation core interactions between dislocation segments and Si atoms that may be studied by atomistic simulations similar as those for Al-Mg alloys [16]. An improved understanding of such reactions is important in order to model the strength and work hardening of Al-Si alloys and ultimately of industrial multi-component solid solution alloys.

Acknowledgement

This work is funded by Research Council of Norway, Hydro and Sapa under the project MOREAL.

References

[1] G.P.M. Leyson, W.A. Curtin, L.G. Hector, C.F. Woodward, Nat. Mater., 9 (2010) 750-755.
[2] G.P.M. Leyson, L.G. Hector Jr., W.A. Curtin, Acta Mater., 60 (2012) 3873-3884.
[3] P. Haasen, Solution hardening in fcc metals, in: F.R.N. Nabarro (Ed.) Dislocations in Solids, North-Holland, New York, 1979, pp. 155-189.
[4] P. Haasen, Mechanical properties of solid solutions, in: R.W. Cahn, P. Haasen (Eds.) Physical Metallurgy (Fourth Edition), North-Holland, Oxford, 1996, pp. 2009-2073.
[5] H. Neuhäuser, C. Schwink, Solid solution strengthening, in: R.W. Cahn, P. Haasen, E.J. Kramer (Eds.) Materials Science and Technology: a comprehensive treatment, Wiley-VCH, Weinheim, 2005.

[6] Ø. Ryen, O. Nijs, E. Sjölander, B. Holmedal, H.E. Ekström, E. Nes, Metall. Mater. Trans. A, 37 (2006) 1999-2006.
[7] T. Mukai, K. Higashi, S. Tanimura, Mater. Sci. Eng., A, 176 (1994) 181-189.
[8] B. Rønning, K. Nord-Varhaug, T. Furu, E. Nes, Mater. Sci. Forum, 331 (2000) 571-576.
[9] J.M. Robinson, M.P. Shaw, Int. Mater. Rev, 39 (1994) 113-122.
[10] G. Rajaram, S. Kumaran, S. Suwas, Mater. Sci. Eng., A, 528 (2011) 6271-6278.
[11] M. Niinomi, T. Kobayashi, K. Ikeda, J. Mater. Sci. Lett., 5 (1986) 847-848.
[12] G. Ghosh, Al-Fe-Si (Aluminium - Iron - Silicon), in: G. Effenberg, S. Ilyenko (Eds.) Light Metal Ternary Systems: Phase Diagrams, Crystallographic and Thermodynamic Data, SpringerMaterials - The Landolt-Börnstein Database, 2008.
[13] Y. Du, Y.A. Chang, B. Huang, W. Gong, Z. Jin, H. Xu, Z. Yuan, Y. Liu, Y. He, F.Y. Xie, Mater. Sci. Eng., A, 363 (2003) 140-151.
[14] H.S. Rosenbaum, D. Turnbull, Acta Metall., 6 (1958) 653-659.
[15] N.Q. Chinh, F. Csikor, Z. Kovacs, J. Lendvai, J. Mater. Res., 15 (2000) 1037-1040.
[16] W. Curtin, D. Olmsted, L. Hector, Nat. Mater., 5 (2006) 875-880.
[17] N. Hansen, Acta Metall., 25 (1977) 863-869.
[18] J. Zander, R. Sandström, L. Vitos, Comput. Mater. Sci., 41 (2007) 86-95.
[19] E. Nes, K. Marthinsen, Y. Brechet, Scr. Mater., 47 (2002) 607-611.
[20] U.F. Kocks, H. Mecking, Prog. Mater. Sci., 48 (2003) 171-273.
[21] O.-G. Lademo, O. Engler, A. Benallal, O.S. Hopperstad, Int. J. Mater. Res, 103 (2012) 1035-1041.

Article 5

Effect of Si addition on Solid Solution Hardening of Al-Mn Alloys*

Qinglong Zhao, Bjørn Holmedal
Department of Materials Science and Engineering, Norwegian University of Science and Technology; Trondheim, N-7491, Norway

Abstract: Non-heat-treatable aluminum alloys owe their strength mainly to elements in solid solution. But the effect of the combination of multiple elements on strength is not well known. Small amounts of Si usually exist in many commercial alloys. Three high purity based Al-Mn binary alloys and one ternary alloy with addition of Si are investigated in this work. The varied solute contents are achieved by cast compositions and the grain structures are controlled by recrystallization. The strength is measured by tensile tests at room temperature. It is found that the addition of Si to Al-Mn alloys leads to a similar increase in strength as adding a similar amount of Mn.

Keywords: Solid solution hardening, high purity aluminum, flow stress

Introduction

Al-Mg and Al-Mn alloys are widely used, and the hardening effect of Mg and Mn in solid solution has been studied (e.g. [1]). Small amounts of Si usually exist in many commercial alloys, and may affect the strength. Tensile [2] and hot deformation experiments [3] of binary Al-Si alloys, and theoretical calculations [4] indicate that Si has a weak hardening effect. However, the effect of the combination of multiple elements on strength is not well known. The total increase of strength is not expected to be linearly dependent on each component [5]. The aim of this work was to investigate the hardening effect of Si addition in high purity Al-Mn binary alloys to study the influence of multiple elements on strength.

* NOTICE: this is the author's version of a work that was presented in ICAA13. The definitive version is published by TMS in Wiley online library. DOI: 10.1002/9781118495292.ch273

Experimental

There Al-Mn binary alloys (BA1, BA2, and BA3) were made of 99.99% pure Al mixed with 99.9% pure Mn in a melting pot at about 800°C. A mold of 7cm×7.5cm×20cm was applied for directed solidification. An Al-Mn-Si ternary alloy (TA) was also made by the addition of Si to one of the binary alloys. The compositions of the alloys are listed in Table I. The cast ingots were homogenized by fast heating (200°C/h) to 635°C, where they were held for 16 hours, and finally water quenched. The cast ingots were rolled from 20mm to 4mm at room temperature. The rolled sheets were recrystallized at various temperatures for 30min in salt bath, and then cold rolled from 4mm to 1mm in thickness. The final recrystallization occurred while the specimens were held for 20min in salt bath (recrystallization temperatures in Table I). The hardness of the annealed samples was measured to determine the recrystallization temperature, and the recrystallized grain sizes were measured by optical microscopy.

The microstructures were observed by back-scattered electron imaging at 15KV in a field emission gun SEM Zeiss Ultra 55 with an EBSD detector. The textures were measured on ND-TD (normal and transverse direction) sections by coarse step EBSD mapping. The sample surfaces were electropolished in a 20% $HClO_4$ ethanol solution at room temperature and 30V for 8s. The recrystallized sheets for tensile tests were 6mm wide and the gauge section was 25mm long. An MTS 810 hydraulic testing machine was run under a constant ramp rate at room temperature, giving a true strain rate of about $10^{-3}s^{-1}$.

Table I. The compositions (mass percent) of alloys, recrystallization temperatures and grain sizes

		Mn	Si	Annealing temperature,ºC	Taylor factor *M*	Grain size,μm
PA	99.99%Al	0.00	<0.01	325	3.0	65
BA1	AlMn0.25	0.22	<0.01	350	2.9	29
BA2	AlMn0.5	0.44	<0.01	350	2.9	25
BA3	AlMn1.0	0.93	<0.01	400	2.7	37
TA	AlMn0.25Si0.1	0.22	0.10	350	3.0	33

Results and discussion

Microstructure And Textures

The microstructure was fully recrystallized (Figure 1) and no particles were observed in SEM. The grain structures of the binary alloys were relatively uniform, while the recrystallization structure of the ternary alloy was less homogeneous, containing fine-grain and coarse-grain bands, as shown in Figure 1. The coarse grain structure corresponds to the very coarse grains of the cast structures.

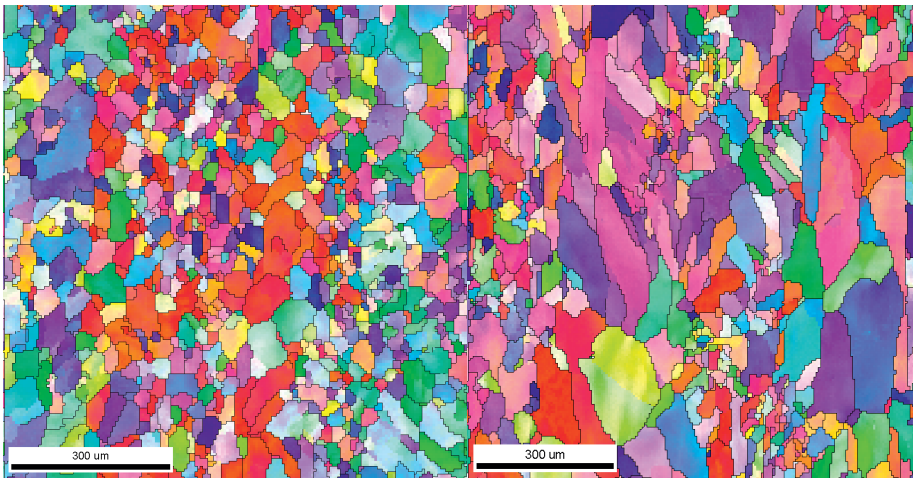

Figure 1. The grain structure of BA1(left) and TA (right).

Textures were measured by coarse step EBSD mapping. Recrystallization resulted in a Cube texture {100}<001> (Figure 2). The textures are slightly different from alloy to alloy, so that the Taylor factors were also slightly changed. Taylor factors calculated are in the range of 2.7-3.0 for all the alloys.

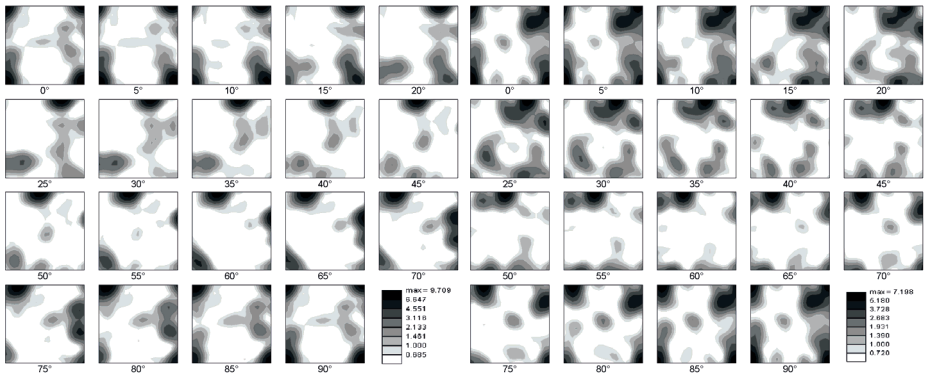

Figure 2. ODF of BA1 (left) and TA (right), showing recrystallization textures

Solid Solution Hardening

The typical stress-strain curves of all the materials are illustrated in Figure 3. Mn solutes increases both the strength of the binary alloys and the work-hardening rate at low strains (<0.1). TA and BA1 have the same Mn level, but the addition of Si leads to the higher strength of TA, although the work-hardening rates of TA and BA1 are similar. The grain size of the binary alloys is small, so the grain size effect on strength is not negligible. It can be estimated by Hall-Petch relation, where the Hall-Petch parameter, k in $kd^{-1/2}$ for high purity Al [6](k=1.27MPa*mm$^{1/2}$) is used in this work.

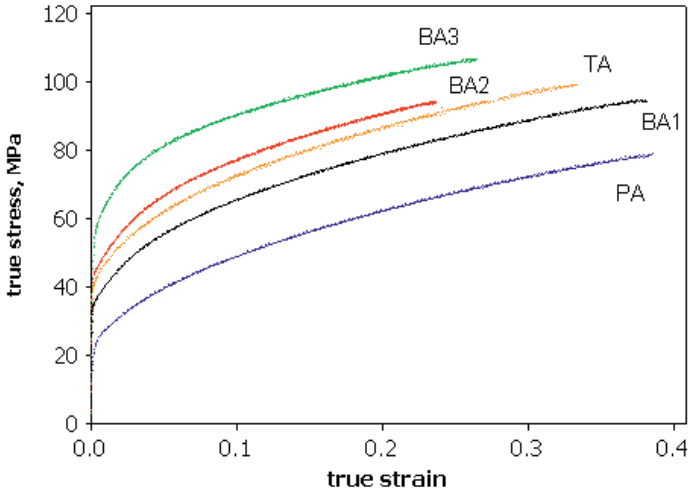

Figure 3. Stress-strain curves at strain rate of $10^{-3}s^{-1}$

Figure 2 shows that the recrystallization textures are slightly different in the alloys, so the Taylor factors vary. The contribution to the critical resolved shear stress (CRSS) caused by the solid solution was calculated from the flow stress by the equation:

$\tau=(\sigma-kd^{-1/2})/M$, (1)

where σ is the true stress, and M is the Taylor factor. The CRSS of the binary alloys at various strain levels is plotted as a function of the atomic concentration of Mn in solid solution in Figure 4. The CRSS of TA are also plotted as a function of Mn concentration in Figure 4. The relation between the CRSS and the Mn content has been expressed:

$\tau=\tau_0+Hc^n$, (2)

where H and n are constants. The parameters in equation (2) for the binary alloys are estimated by fitting the plot in Figure 4, and are listed in Table II. The difference between τ_0 and τ_{PA} is negligible, indicating all the increase in stress are due to the solutes. The solute hardening exponent n for 99.99% purity Al-Mn binary alloys is about 0.8-0.9, similar to that of the 99.999% purity Al-Mn binary alloys reported in [1]. Thus, this work confirms the slightly weaker hardening effect of Mn in high purity binary alloys as compared to the commercial purity 3xxx alloys reported in [1].

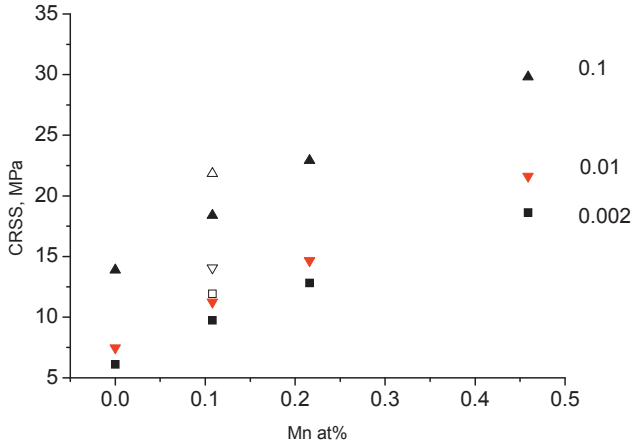

Figure 4. Shear stress at various strains (0.002, 0.01, and 0.1) as a function of Mn content in solid solution (the binary alloys, solid symbols; the ternary alloy TA, open symbols)

Table II parameters in equation (2) of high purity Al-Mn binary alloys

strain	τ_{PA}	τ_0	H	n
0.002	6.11	6.09	24.2	0.84
0.01	7.46	7.45	28.7	0.91
0.1	13.89	13.82	30.4	0.82

Tensile tests of high purity Al-0.2Si binary alloys [2] showed that the 0.2% proof stress increased by 4MPa compared to pure Al due to 0.2at%Si. The addition of 0.1at%Si into BA1 increased the 0.2% proof stress by 6.7MPa compared to BA1, suggesting that the hardening effect of Si in multi-component alloys is much stronger than in binary Al-Si alloys. It can be assumed that Si atoms act as equivalent Mn atoms, which means a Si atom multiplied by a coefficient, R_{Si}, has the same hardening effect as a Mn atom. The

coefficient R_{Si} for the flow stress of TA is 0.8-0.9 by fitting it into the trend of the binary alloys, suggesting that Si has a similarly strong hardening effect in the ternary Al-Mn-Si alloy as Mn has in the binary Al-Mn alloys. Ryen et al [1] concludes that Mn has much stronger hardening effect than Mg in solid solution. The hot deformation experiments [3] and theoretical calculations [4] indicate that Si has a much weaker effect than Mg. Thus, a small addition of Si was expected to affect the strength of the Al-Mn alloys very little. However, the ternary alloy behaves opposite the expectation. A possible explanation is that Si has a synergy effect with Mn, leading to a stronger effect than the linear sum of the concentrations. This would also explain the stronger Mn hardening in the commercial purity alloys than in the high purity binary alloys [1].

Conclusions

Manganese in solid solution of high purity alloys gives rise to a concentration dependency of strength in the power of 0.8-0.9, and a small addition of Si to the Al-Mn alloys leads to a similar increase in strength as adding a similar amount of Mn. Synergy effect between Si and Mn is a possible explanation to the significant increase in strength of the Al-Mn-Si ternary alloys.

Acknowledgement

This work is funded by the Research Council of Norway, Hydro and Sapa under the project MOREAL.

References

[1] Ryen Ø, Nijs O, Sjölander E, Holmedal B, Ekström HE, Nes E, "Strengthening mechanisms in solid solution aluminum alloys," *Metallurgical and Materials Transactions A: Physical Metallurgy and Materials Science*, 37 (2006), 1999-2006.
[2] Mahon GJ, Marshall GJ, "Microstructure property relationships in O-temper foil alloys," *Jom-Journal of the Minerals Metals & Materials Society*, 48 (1996), 39-42.
[3] Rønning B, Nord-Varhaug K, Furu T, Nes E, "Effect of chemical composition and microstructure on the flow stress during hot deformation of aluminum alloys," *Materials Science Forum*, 331 (2000), 571-576.
[4] Leyson GPM, Curtin WA, Hector LG, Woodward CF, "Quantitative prediction of solute strengthening in aluminium alloys," *Nature Materials*, 9 (2010), 750-755.
[5] Gypen LA, Deruyttere A, "Multi-component solid solution hardening - Part 1 Proposed model," *Journal of Materials Science*, 12 (1977), 1028-1033.
[6] Hansen N, "The effect of grain size and strain on the tensile flow stress of aluminium at room temperature," *Acta Metallurgica*, 25 (1977), 863-869.